# UCLA
## UCLA Previously Published Works

**Title**

The Vertical Vorticity Structure within a Squall Line Observed during BAMEX: Banded Vorticity Features and the Evolution of a Bowing Segment

**Permalink**

https://escholarship.org/uc/item/71q4j0ww

**Authors**

Wakimoto, Roger M
Stauffer, Phillip
Lee, Wen-Chau

# The Vertical Vorticity Structure within a Squall Line Observed during BAMEX: Banded Vorticity Features and the Evolution of a Bowing Segment

ROGER M. WAKIMOTO

*Department of Atmospheric and Oceanic Sciences, University of Colorado Boulder, Boulder, Colorado*

PHILLIP STAUFFER AND WEN-CHAU LEE

*National Center for Atmospheric Research,* * *Boulder, Colorado*

## ABSTRACT

A quasi-linear convective line with a trailing stratiform region developed during the Bow Echo and Mesoscale Convective Vortex Experiment (BAMEX) while being sampled by two airborne Doppler radars. The finescale reflectivity and Doppler velocities recorded by the radars documented the evolution of the convective line. Bands of positive and negative vertical vorticity oriented parallel to the convective line were resolved in the analysis. This type of structure has rarely been reported in the literature and appears to be a result of the tilting and subsequent stretching of ambient horizontal vorticity produced by the low-level wind shear vector with a significant along-line component. The radar analysis also documented the evolution of an embedded bow echo within the convective line. Embedded bow echoes have been documented for a number of years; however, a detailed analysis of their kinematic structure has not been previously reported in the literature. The counterrotating circulation patterns that are characteristic of bow echoes appeared to be a result of tilting and stretching of the horizontal vorticity produced in the cold pool. The analysis suggests that the location along the convective line where embedded bow echoes form depends on the local depth of the cold pool. The rear-inflow jet is largely driven by the combined effects of the counterrotating vortices and the upshear-tilted updraft.

## 1. Introduction

The vertical vorticity structure has been shown to significantly influence the evolution of mesoscale convective systems (e.g., Verlinde and Cotton 1990; Bartels and Maddox 1991; Biggerstaff and Houze 1991b; Weisman 1993; Davis and Weisman 1994; Skamarock et al. 1994; Weisman and Davis 1998; Davis and Trier 2002). Previous studies have shown a wide variety of vortices that vary in horizontal dimensions and exist for hours to several days. Indeed, long-lived circulation patterns (e.g., mesoscale convective vortices; MCVs) can exist beyond the life cycle of the parent convective system.

They are often manifested as a large-scale balanced midlevel circulation (100–600 km in diameter), are typically found in the stratiform region of convective systems (e.g., Houze et al. 1989, 1990), and can initiate new convection on subsequent days (e.g., Bosart and Sanders 1981; Bartels and Maddox 1991; Fritsch et al. 1994). This vortex is such a dominant feature within these systems that other system-wide vorticity structures have received less attention in the literature. Biggerstaff and Houze (1991a,b) were the first to document prominent bands or ribbons of positive and negative vertical vorticity oriented parallel to the convective line and extending into the stratiform region. Their results were based on a composite analysis of dual-Doppler data, rawindsonde winds, wind profilers, and surface mesonet observations that were digitized onto a $15 \times 15\,\mathrm{km}^2$ grid and filtered to remove wavelengths less than 60 km. A model simulation of the same storm by Zhang et al. (1989) replicated the banded structure. Biggerstaff and Houze (1991b) hypothesized that coarse horizontal resolution may have prevented past studies from documenting

this kinematic structure. However, to the authors' knowledge, there has been no subsequent observational study that has documented a similar event even with the availability of higher spatial resolution data collected by both mobile ground-based and airborne Doppler radars.

Smaller-scale vortices that occur within quasi-linear convective systems (i.e., a mesoscale system associated with a convective line that is approximately linear) have also been documented by a number of researchers. These vortices often develop as counterrotating circulations and can locally enhance the strength of rear-inflow jets (e.g., Smull and Houze 1987; Weisman 1992) and are characteristic features of bow echoes (e.g., Fujita 1981; Weisman 2001). Weisman (1993) referred to these circulations as bookend or line-end vortices. Bow echoes are observed over a range of scales from tens to a few hundred kilometers (Klimowski et al. 2004). Bow echoes can occur as isolated features or as smaller-scale bow-shaped segments or "embedded" bow echoes within a larger squall line (e.g., Johns and Hirt 1987; Przybylinski 1995). Weisman and Davis (1998) coined the term subsystem-scale vortices for the circulations associated with these bowing segments. These segments are typically 15–40 km in length and were more recently modeled by James et al. (2006). Although these bow-shaped segments have been recognized to exist for a number of years, there has been no detailed observational study that has examined this type of event to date.

On 2 June 2003, a quasi-linear convective line with a trailing stratiform region developed over Mississippi while being sampled by two airborne Doppler radars during the Bow Echo and MCV Experiment (BAMEX; Davis et al. 2004). The radars on board the aircraft collected finescale reflectivity and Doppler velocities that documented the evolution of the convective line. Section 2 describes BAMEX and the research aircraft deployed during the experiment. The environmental conditions, a description of the quasi-linear convective system, and the coordination of the aircraft while collecting data on the event are presented in section 3. The results of the radar analyses are shown in section 4 and a summary and discussion are presented in section 5.

## 2. BAMEX and the aircraft

One of the major objectives of the BAMEX field campaign was to collect data on the life cycle of bow-echo systems that are associated with damaging winds at the surface [sometimes called derechoes; Johns and Hirt (1987)]. The field phase of the experiment was the spring and summer of 2003 and was based at MidAmerica

TABLE 1. ELDORA scanning mode.

| | |
|---|---|
| Antenna rotation rate ($°\,s^{-1}$) | 140 |
| No. of samples | 24 |
| PRF (Hz) | 2000/2500 |
| Gate length (m) | 150 |
| Sweep-angle beam spacing (°) | 1.4 |
| Along-track data spacing (m) | ~300 |
| Max range (km) | 60 |
| Max unambiguous velocities ($\pm m\,s^{-1}$) | 77.2 |
| Min detectable signal at 10 km (dB$Z$) | ~−15 |

Airport located east of St. Louis, Missouri. The primary platforms used in the current study are two airborne Doppler radars that have been used extensively to study convective and mesoscale phenomena, including hurricanes. The Electra Doppler Radar (ELDORA) is a 3-cm airborne Doppler radar that is operated by the National Center for Atmospheric Research (NCAR). ELDORA is equipped with two flat-plate antennas mounted back to back that scan vertically and are directed slightly fore and aft of normal to the fuselage of the aircraft by ~18.5°. ELDORA uses a multiple-beam scanning technique in order to collect data that can be used in a dual-Doppler wind synthesis. The fore and aft beams intersect with a spacing of ~300 m in the along-track direction under nominal flying conditions. Table 1 presents a list of ELDORA's scanning parameters used during BAMEX. There is a time lag between intersecting fore and aft beams that are used in a dual-Doppler wind synthesis. An aircraft ground speed of ~120 m s$^{-1}$ results in a lag of ~1 min (10 km)$^{-1}$ of range. For example, if a storm was ~15 km from the aircraft, the time lag would be 90 s. The storm evolution is assumed to be stationary during this lag and is typical for dual-Doppler wind syntheses. For more information regarding ELDORA, the interested reader is referred to Hildebrand et al. (1994, 1996). The National Oceanic and Atmospheric Administration (NOAA) operates a P-3 aircraft that is also equipped with an airborne (3 cm) Doppler radar (Jorgensen et al. 1983). The scanning technique is similar to the one used by ELDORA; however, the along-track data spacing is greater owing to the slower antenna scan rate. The fore–aft scanning angle is 20°. The scanning parameters used by the radar on board the NOAA P-3 are shown in Table 2.

The main flight plan for ELDORA was to fly along and ahead of the convective line (to the east of the line in this case) in a racetrack pattern at low levels [~1.6 km above ground level (AGL); hereafter, all heights are AGL]. The NOAA P-3 flew to the rear of the line (to the west) and within the trailing stratiform region where rear inflow and the bookend vortices commonly develop (Davis et al. 2004; see their Fig. 2). The two aircraft

TABLE 2. NOAA P-3 tail radar scanning mode.

| | |
|---|---|
| Antenna rotation rate ($°\,s^{-1}$) | 60 |
| No. of samples | 32 |
| PRF (Hz) | 2133/3200 |
| Gate length (m) | 150 |
| Sweep-angle beam spacing (°) | 0.75 |
| Along-track data spacing (m) | ~1200 |
| Max range (km) | 46.8 |
| Max unambiguous velocities ($\pm\,m\,s^{-1}$) | 51.5 |
| Min detectable signal at 10 km (dBZ) | ~0 |

attempted to synchronize their flight tracks during missions whenever possible so that radar data could be nearly simultaneously collected such that a quad-Doppler wind synthesis could be performed (Jorgensen et al. 1996). The quad-Doppler technique reduces the uncertainty of the derived vertical velocities in the overlapping region where both radars are sampling since vertical velocities at echo top can be estimated rather than having to assume $w = 0\,m\,s^{-1}$ at echo top for the vertical integration of divergence (Jorgensen et al. 1996). Merging of the two radar datasets also results in a Doppler wind synthesis that extends over a larger region. A total of seven flight legs were completed on the 2 June storm. The two aircraft were able to coordinate on four of these legs. A description of the airborne Doppler wind synthesis used for this study is presented in the appendix. The complete BAMEX dataset is available online (http://data.eol.ucar.edu/master_list/?project=BAMEX).

## 3. Environmental conditions, overview of the quasi-linear convective system, and the aircraft flight legs

Initial thunderstorm activity could be tracked back to Colorado on 1 June. The region of convective activity moved southeastward through Kansas, Oklahoma, and into Arkansas (not shown). Squall-line features formed and dissipated as the system moved into western Mississippi. Indeed, thunderstorms were widely scattered between 2130 and 2200 UTC before organizing into a quasi-linear convective system as it entered into northwest Mississippi. The convective line moved along a warm front as suggested by Johns and Hirt (1987) and Johns (1993) and into a region where convective available potential energy (CAPE) values were greater than $2000\,J\,kg^{-1}$. An upper-level short-wave trough was propagating through Oklahoma and Texas to the west of the warm front (not shown). The CAPE estimated from a sounding launched in advance of the convective line at 1903 UTC (Fig. 1) was $2001\,J\,kg^{-1}$.
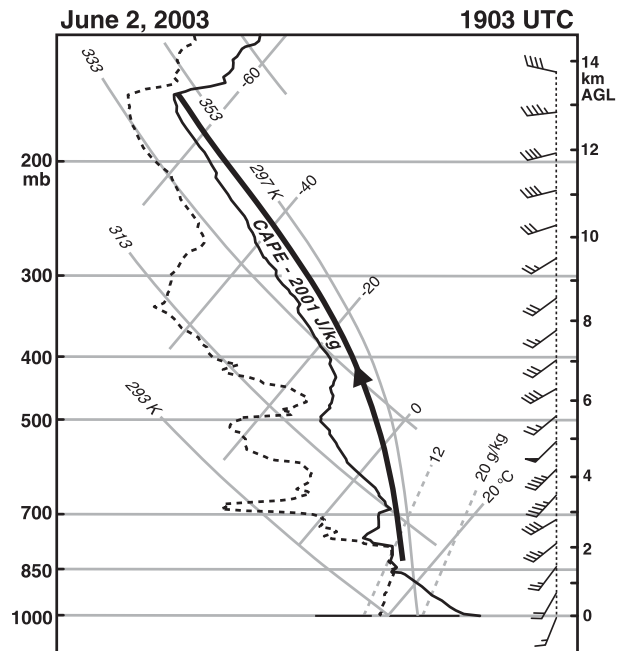


FIG. 1. Sounding launched at 1903 UTC 2 Jun 2003. Location of the launch is shown in Fig. 3.

The low-level wind shear was examined based on the sounding shown in Fig. 1, a nearby wind profiler, and a number of velocity azimuth display (VAD) analyses from the Doppler velocity data collected by the Weather Surveillance Radar-1988 Doppler (WSR-88D) at Columbus Air Force Base, Mississippi (KGWX). The profiler and VAD analysis provided a consistent estimate of the low-level wind shear vector pointing to the northeast (Fig. 2). The magnitudes of the CAPE and wind shear depicted in Figs. 1 and 2 are within the range that could support bow echoes (e.g., Evans and Doswell 2001; Coniglio et al. 2004). The wind profile based on the sounding shown in Fig. 1 was excluded since it did not depict the southeasterly flow at the surface that was apparent in the other wind profiles and the analyses of the surface winds in eastern Arkansas and northern Mississippi (not shown).

The outline of the quasi-linear convective line at 2306:00–2325:00 UTC is also plotted in Fig. 2 and illustrates that a component of the low-level shear vector was parallel to the convective line. The relationship between the squall-line orientation and the low-level shear vector has received a great deal of attention in the literature. The tendency for the low-level shear vector to align perpendicular to convective lines has been noted (e.g., Rotunno et al. 1988; Weisman et al. 1988; Keenan and Carbone 1992; Fankhauser et al. 1992; Weisman 1993; Robe and Emanuel 2001). However, convective lines can also be associated with a significant component
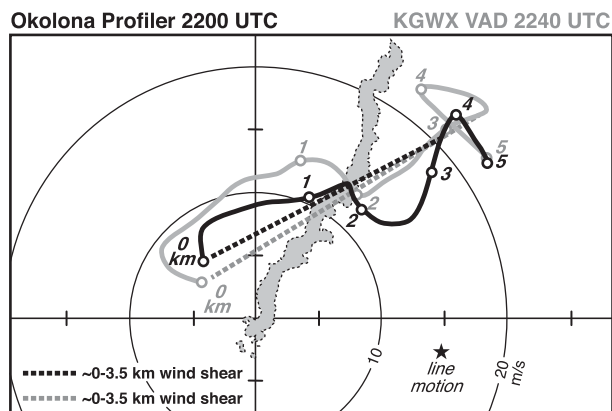
FIG. 2. Hodographs showing the 0–3.5 km AGL shear based on data from the Okolona, MS, profiler at 2200 UTC (black line) and a VAD analysis of the KGWX WSR-88D data at 2240 UTC (gray line). The black dashed and gray dashed lines represent the approximate 0–3.5-km shear based on the profiler and radar data, respectively. Radar reflectivities greater than 35 dB$Z$ at 2306:00–2325:00 UTC are shaded gray. The star represents the convective line motion. Location of the Okolona profiler is shown in Fig. 3.

of the low-level wind shear along the line (e.g., Bluestein and Jain 1985; Parker and Johnson 2000).

A sequence of low-level scans from the nearby KGWX radar is presented in Fig. 3. The plots reveal that the mesoscale convective system was characterized by a quasi-linear convective line associated with a transition zone and trailing stratiform region during the data collection period. The line movement shown in Fig. 3 was ~15 m s$^{-1}$ from 260° based on tracking of the line using the KGWX data. The arrow (Fig. 3g) denotes the location where a small-scale bow echo (hereafter referred to as bow echo) developed and will be discussed in detail in section 4b. Strong winds (sustained speeds greater than 30 m s$^{-1}$) and minor damage were reported as the bowing segment moved into eastern Mississippi. Also plotted in Fig. 3 are the flight tracks of ELDORA and the NOAA P-3. The convective line was sampled by the airborne platforms for over 2 h, providing a good time history of the convective system and also documenting the formation of the bow echo. As previously mentioned, the two aircraft were able to fly in a coordinated manner on four of the seven flight legs (shown in Figs. 3a, 3c, 3f, and 3g). The aircraft flight legs were nominally 100 km in length, resulting in analyses that could resolve the detailed kinematic structure of the convective line over an extended path. The main disadvantage was the time required to execute one leg (15–17 min), which decreased the temporal resolution. The elapsed time between the intersecting beams of the two aircraft was also a limiting factor. However, sampling along a flight leg also

provides a unique opportunity to average a number of vertical cross sections along the convective line, resulting in a representative profile of the mean kinematic flow.

## 4. Multiple Doppler analyses

A total of seven analysis times of the quasi-linear convective line using data collected with ELDORA were available for the current study. Data collected by both ELDORA and the NOAA P-3 were available during four of the seven legs. Accordingly, the dataset collected in the present study documented the overall structure and evolution of the convective line for an extended period. The wind synthesis was also used to document the finescale structure of a bow echo that developed within the line.

### a. Overall structure of the quasi-linear convective system

#### 1) 2214:18–2229:00 UTC

The first analysis of the convective line combining the wind syntheses of both ELDORA and the NOAA P-3 radars is from 2214:18 to 2229:00 UTC (Fig. 4a). The quality of the quad-Doppler wind synthesis at the southern end of the analysis domain was a concern. The time difference between the data collected by the two radars was 13–14 min since the aircraft were flying in opposite directions. A second wind synthesis was created (not shown) using only the data recorded by the NOAA P-3 radar and was compared with the kinematic fields shown in Fig. 4 in order to examine the impact of this time difference. These two wind syntheses and derived fields were nearly identical, such that the conclusions based on the analysis presented in Fig. 4 would not have changed.

An examination of all of the wind syntheses created for this study revealed that the vertical vorticity features were well defined at the 2.25-km level. There is general southeasterly storm-relative flow ahead of the convective line (Fig. 4a). The flow to the rear of the convective line reveals weak southwesterly flow followed by a region of stronger northeasterly winds before the winds turn to become southerly to southwesterly much farther to the west. This alternating pattern in the wind field is consistent with the distinct bands of vertical vorticity (Fig. 4b), starting with a ribbon of cyclonic vorticity within the convective line, followed by anticyclonic, cyclonic, and anticyclonic bands farther into the stratiform region. There is also a band of anticyclonic vorticity out ahead of the convective line.
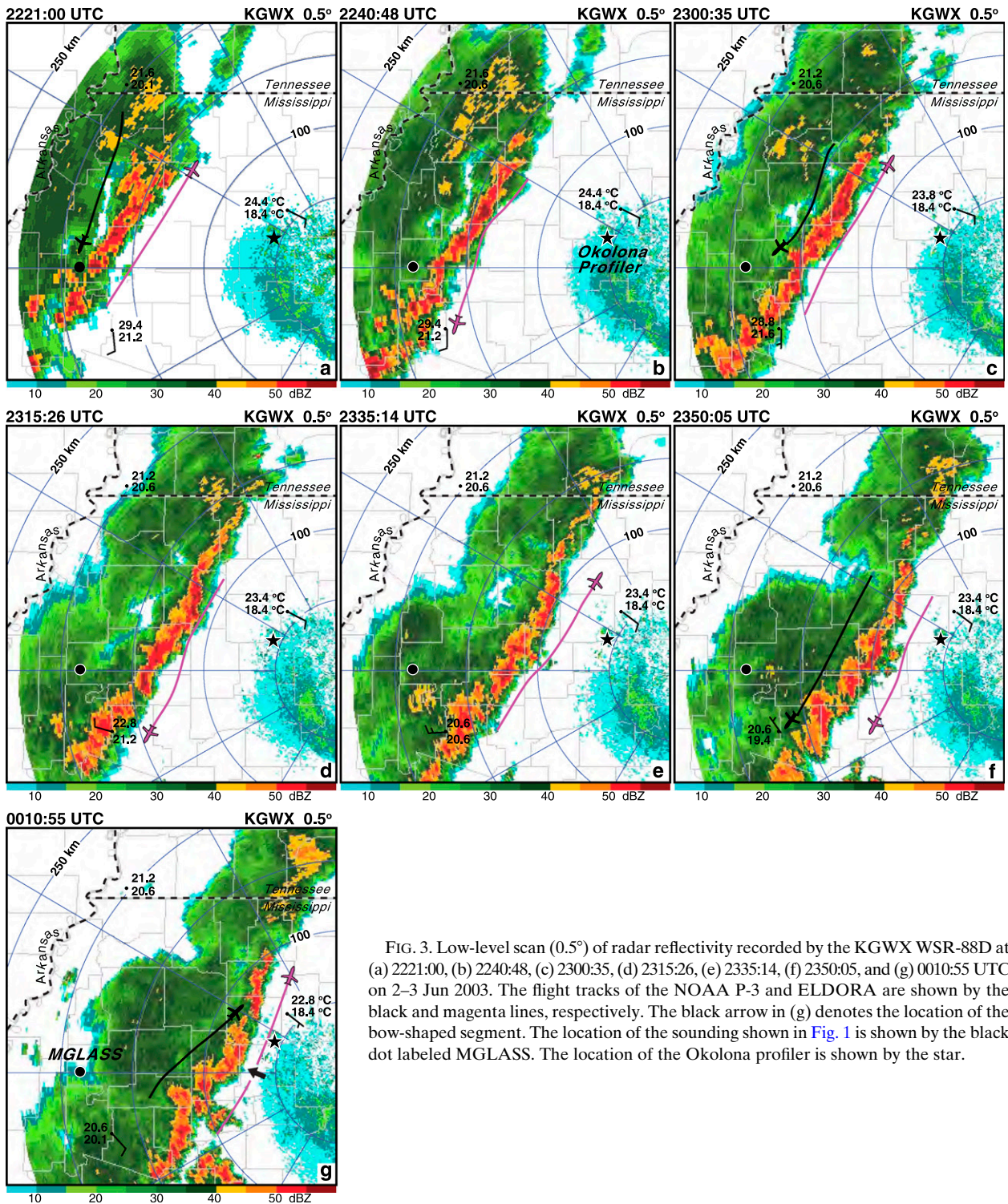
FIG. 3. Low-level scan (0.5°) of radar reflectivity recorded by the KGWX WSR-88D at (a) 2221:00, (b) 2240:48, (c) 2300:35, (d) 2315:26, (e) 2335:14, (f) 2350:05, and (g) 0010:55 UTC on 2–3 Jun 2003. The flight tracks of the NOAA P-3 and ELDORA are shown by the black and magenta lines, respectively. The black arrow in (g) denotes the location of the bow-shaped segment. The location of the sounding shown in Fig. 1 is shown by the black dot labeled MGLASS. The location of the Okolona profiler is shown by the star.

The present BAMEX study was able to examine the structure of these vorticity features shown in Fig. 4a with high temporal and spatial resolution. Biggerstaff and Houze (1991a,b) used a composite analysis of several

data sources over an approximate 3-h period. In addition, the widths of the individual bands documented in their study were ~60 km, much greater than the organization shown in Fig. 4b. Zhang et al. (1989)
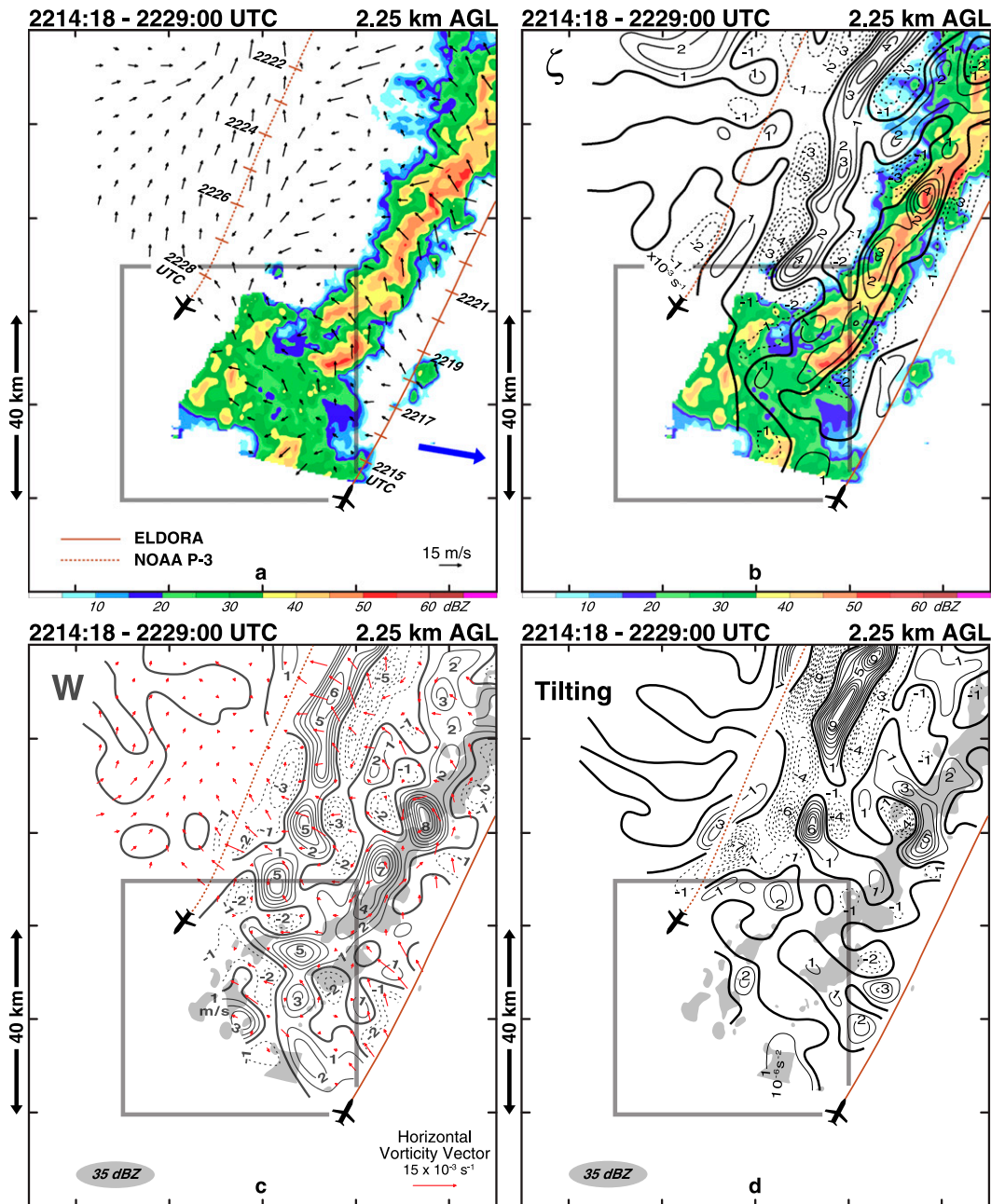
FIG. 4. Wind synthesis at 2214:18–2229:00 UTC at 2.25 km AGL. (a) Storm-relative winds and radar reflectivity. (b) Vertical vorticity ($\times 10^{-3}$ s$^{-1}$) and radar reflectivity. (c) Horizontal vorticity vectors, vertical velocity, and radar reflectivities >35 dB$Z$ are shaded gray. (d) Tilting term ($\times 10^{-6}$ s$^{-2}$) and radar reflectivities >35 dB$Z$ shaded gray. ELDORA and the NOAA P-3 flight tracks are shown by the solid and dashed brown lines, respectively. Positive and negative values of vertical vorticity, vertical velocity, and tilting term are shown by the solid and dashed black lines, respectively. The gray box is enlarged in Fig. 10. Blue arrow in (a) denotes the convective line motion.

performed a numerical simulation of the same squall line and appeared to replicate the banded structure shown in Biggerstaff and Houze (1991a,b). Trier et al. (1997) simulated a tropical squall line that also exhibited a band of cyclonic vorticity followed by an anticyclonic band (see their Fig. 16), although it is not discussed since their focus was on the formation of line-end vortices. Weckwerth and Wakimoto (1992) documented banded vorticity structures parallel to an outflow boundary and atop a cold pool that

appeared to be in association with internal gravity waves.

The vertical velocity field (Fig. 4c) for this time reveals a banded structure, which suggests that tilting of horizontal vorticity could be playing a role in creating the observed vertical vorticity field. The contribution of tilting and stretching to the total change in vertical vorticity can be written as

$$\frac{d\zeta}{dt} = -\underbrace{\left(\frac{\partial w}{\partial x}\frac{\partial v}{\partial z} - \frac{\partial w}{\partial y}\frac{\partial u}{\partial z}\right)}_{\text{tilting}} - \underbrace{\zeta\left(\frac{\partial u}{\partial x} + \frac{\partial v}{\partial y}\right)}_{\text{stretching}}, \qquad (1)$$

where $\zeta$ is the vertical vorticity and $u$, $v$, and $w$ are the velocity components. The horizontal vorticity vectors out ahead of the convective line (Fig. 4c) are pointing to the northwest consistent with the low-level shear depicted in the hodograph (Fig. 2). Accordingly, there is a significant component of the vector that is perpendicular to the line. The combination of the vertical velocity field and the tilting term (Fig. 4d) is consistent with the vertical vorticity analysis based on (1).

The vertical cross section oriented in a direction perpendicular to the convective line is presented in Fig. 5. The results shown in Fig. 5 depict the mean vertical structure by averaging individual cross sections from the Doppler wind syntheses along the entire length of the flight track. The horizontal grid spacing of the analysis was 1.2 km (see the appendix). Accordingly, mean vertical cross sections were produced by averaging ~125 individual cross sections for each flight leg. The averaging was effective in removing the along-line variability.

The storm-relative flow and radar reflectivity profiles (Figs. 5a,b) are consistent with midlatitude mesoscale convective systems documented in the literature (e.g., Houze et al. 1989). A leading convective line followed by a transition zone and stratiform region with a bright band are apparent. An ascending front-to-rear flow starting within the main convective updraft is evident in the cross section although no rear inflow can be identified at this time. The vertical velocity field and vorticity vectors shown in Fig. 5c strongly suggest tilting as the primary mechanism for the banded vertical vorticity structure shown in Fig. 4b. This is further supported by the comparison of the tilting and vertical vorticity plots (Fig. 5d). There appear to be three general areas of downward motion depicted in the mean cross sections (Fig. 5c). The first is the low-level downdraft within the leading convective line. Downdrafts are also noted within the transition zone and near the bright band associated with the region of stratiform precipitation. The latter two downdrafts have been well documented (e.g., Biggerstaff and Houze 1991b). In addition, another

downdraft is apparent ahead of the convective region and represents compensating subsidence of the strong convective line updrafts (Hoxit et al. 1976; Sun et al. 1993; Houze et al. 1989). This downdraft contributes to the development of the anticyclonic band of vorticity ahead of the convective line by the downward tilting of the ambient horizontal vorticity.

The results presented in Figs. 4 and 5 are consistent with the vorticity structure presented by Biggerstaff and Houze (1991b) with two differences: the tilting of the horizontal vorticity by the low-level convective downdraft and the downdraft associated with compensating subsidence. If these features were present in their study, the coarser-resolution analyses would likely not have been able to resolve them.

2) 2231:00–2248:00, 2308:00–2325:00, AND 0002:45–0017:30 UTC

The second pass along the leading edge of the convective line only included data collected by ELDORA (Fig. 3b). The major difference in the echo structure from the previous analysis time is noted along the southern section of the convective system. Scattered cells have organized and extended the line to the south (Fig. 6a). The absence of data collected by the NOAA P-3 limits the analysis in the stratiform region in Fig. 6; however, the band of cyclonic vorticity followed by a band of anticyclonic vorticity is still evident (Fig. 6b). The area of anticyclonic vorticity is still apparent out ahead of the convective line but is limited to two small regions of negative vorticity ($< -1 \times 10^{-3}\,\text{s}^{-1}$). The mean vertical cross section at this time (not shown) is consistent with the results presented in the previous section. Tilting of the vorticity vector by the low-level convective downdraft and subsidence downdraft in concert with the main convective updraft (Fig. 6c) support the observed vertical vorticity structure. The stretching term added to the tilting effect (Fig. 6d) is consistent with the vertical vorticity plot shown in Fig. 6b. The kinematic structure of the convective line during the third analysis time (2250–2305 UTC; not shown) is similar to the previous pass.

The band of cyclonic (and followed by anticyclonic) vertical vorticity is still apparent by the fourth pass by ELDORA at 2308–2325 UTC (Fig. 7b). The main updraft along the convective line followed by the low-level convective downdraft continued to be prominent features in the kinematic fields (Fig. 7c). The plot that combines the effects of the tilting and stretching terms (Fig. 7d) reveals a pattern that is different than what was shown in Fig. 6d. The areas of positive and negative tilting and stretching no longer suggest a banded structure along the line. Instead the maximum–minimum
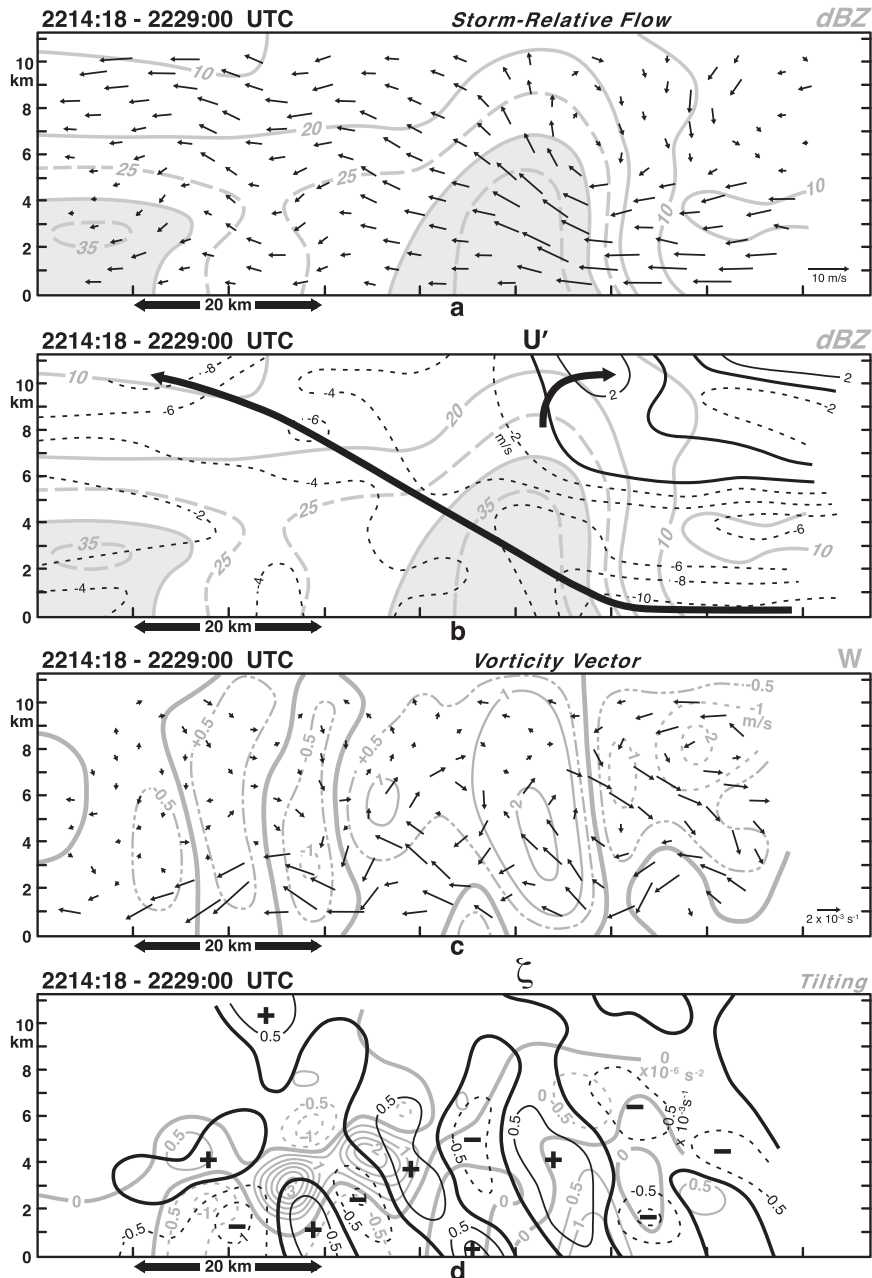
FIG. 5. Vertical cross section perpendicular to the convective line at 2214:18–2229:00 UTC depicting (a) storm-relative flow and radar reflectivity, (b) the component of storm-relative flow perpendicular to the convective line ($U'$) and radar reflectivity, (c) vorticity vector in the plane of the cross section and vertical velocity, and (d) vertical vorticity and tilting term. The variables are based on an average of 125 vertical cross sections along the entire length of the convective line resolved in the wind synthesis. Black arrows in (b) depict approximate flow pattern as shown in (a). To resolve areas characterized by weak gradients in (c), the 0.5 and $-0.5\,\mathrm{m\,s^{-1}}$ isopleths have been added with dash–dot and dash–dot–dot lines, respectively.

features depict a more three-dimensional pattern. The results shown in Fig. 7d represent the tendencies of vertical vorticity and suggest that future plots of vertical vorticity will also evolve into a structure that will depart

from the banded features. An example of this transition can be seen in the boxed-in area shown in Fig. 7a. The storm-relative wind field depicts two counterrotating circulation patterns that are characteristic features of a bow
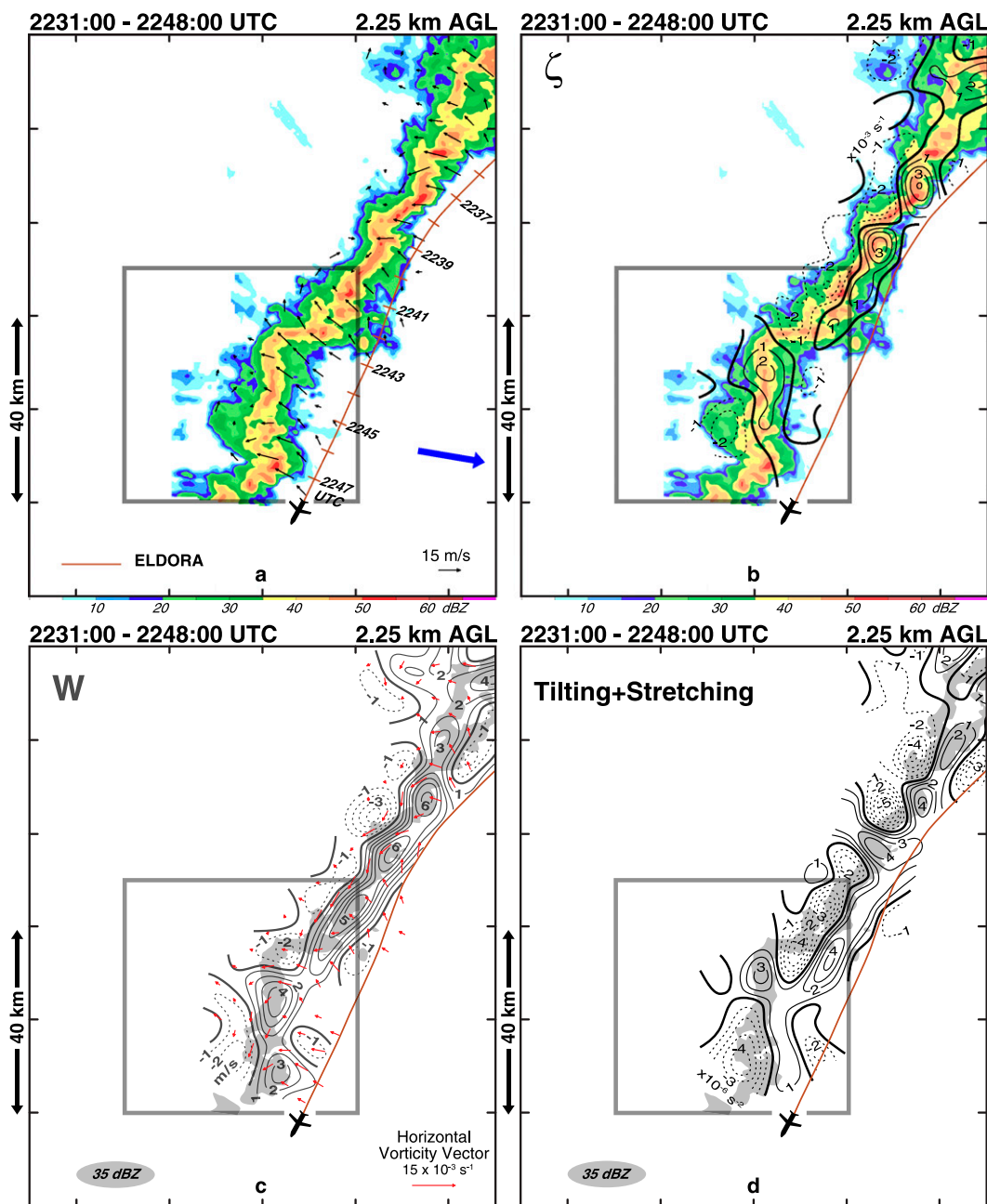
FIG. 6. Wind synthesis at 2231:00–2248:00 UTC at 2.25 km AGL. (a) Storm-relative winds and radar reflectivity. (b) Vertical vorticity ($\times 10^{-3}\,\mathrm{s}^{-1}$) and radar reflectivity. (c) Horizontal vorticity vectors, vertical velocity, and radar reflectivities >35 dB$Z$ shaded gray. (d) Tilting plus stretching terms ($\times 10^{-6}\,\mathrm{s}^{-2}$) and radar reflectivities >35 dB$Z$ shaded gray. ELDORA flight track is shown by the solid brown lines. Positive and negative values of vertical vorticity, vertical velocity, and tilting plus stretching terms are shown by the solid and dashed black lines, respectively. The gray box is enlarged in Fig. 11. Blue arrow in (a) denotes the convective line motion.

echo (e.g., Weisman 1993; Jorgensen et al. 1997). The circulations are supported by a couplet of anticyclonic and cyclonic vorticity (denoted by the black arrows in Fig. 7b), which are also collocated with minimum and maximum centers of tilting and stretching, respectively.

The evolution of the bow echo will be discussed in detail in section 4b.

The convective line continues to evolve into a more three-dimensional pattern during the fifth and sixth analysis times (not shown). The two airborne Doppler
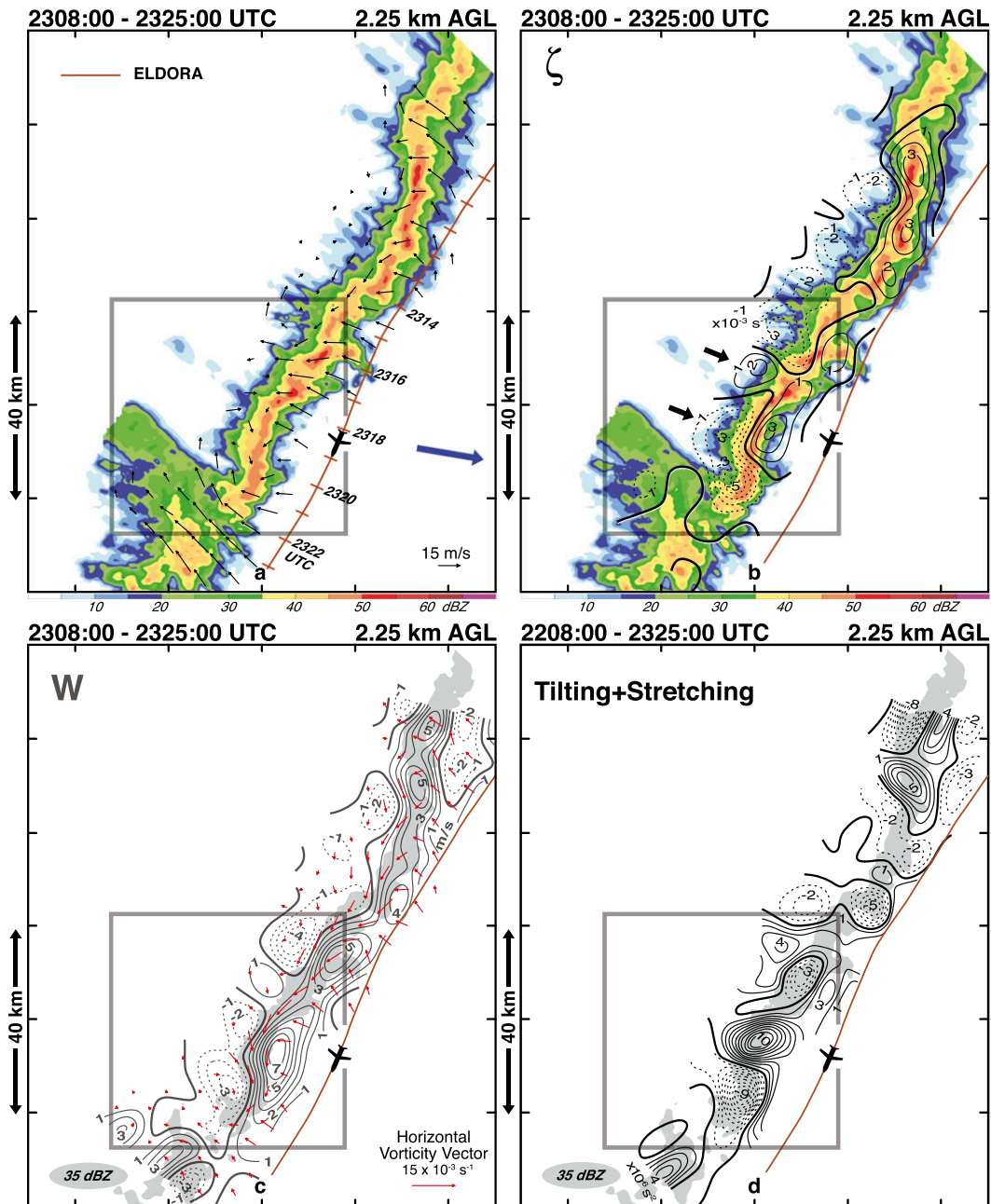
FIG. 7. Wind synthesis at 2308:00–2325:00 UTC at 2.25 km AGL. (a) Storm-relative winds and radar reflectivity. (b) Vertical vorticity ($\times 10^{-3}\,\mathrm{s}^{-1}$) and radar reflectivity. (c) Horizontal vorticity vectors, vertical velocity, and radar reflectivities $>35\,\mathrm{dB}Z$ shaded gray. (d) Tilting plus stretching terms ($\times 10^{-6}\,\mathrm{s}^{-2}$) and radar reflectivities $>35\,\mathrm{dB}Z$ shaded gray. ELDORA flight track is shown by the solid brown lines. Positive and negative values of vertical vorticity, vertical velocity, and tilting plus stretching terms are shown by the solid and dashed black lines, respectively. The gray box is enlarged in Fig. 13a. Blue arrow in (a) denotes the convective line motion. Black arrows in (b) denote a couplet of cyclonic and anticyclonic vertical vortices.

radars were able to coordinate during the seventh pass by the convective line at 0002–0017 UTC. The bow echo is enclosed by the box in Fig. 8a. The rear inflow is evident and is flanked by the two counterrotating vorticity circulations (black arrows in Fig. 8b). The

main updraft and downdraft structure noted at all three previous times presented is still apparent (Fig. 8c). Further to the rear, however, the banded structure of vertical motion no longer exists. The tilting and stretching field in the stratiform region (Fig. 8d) is
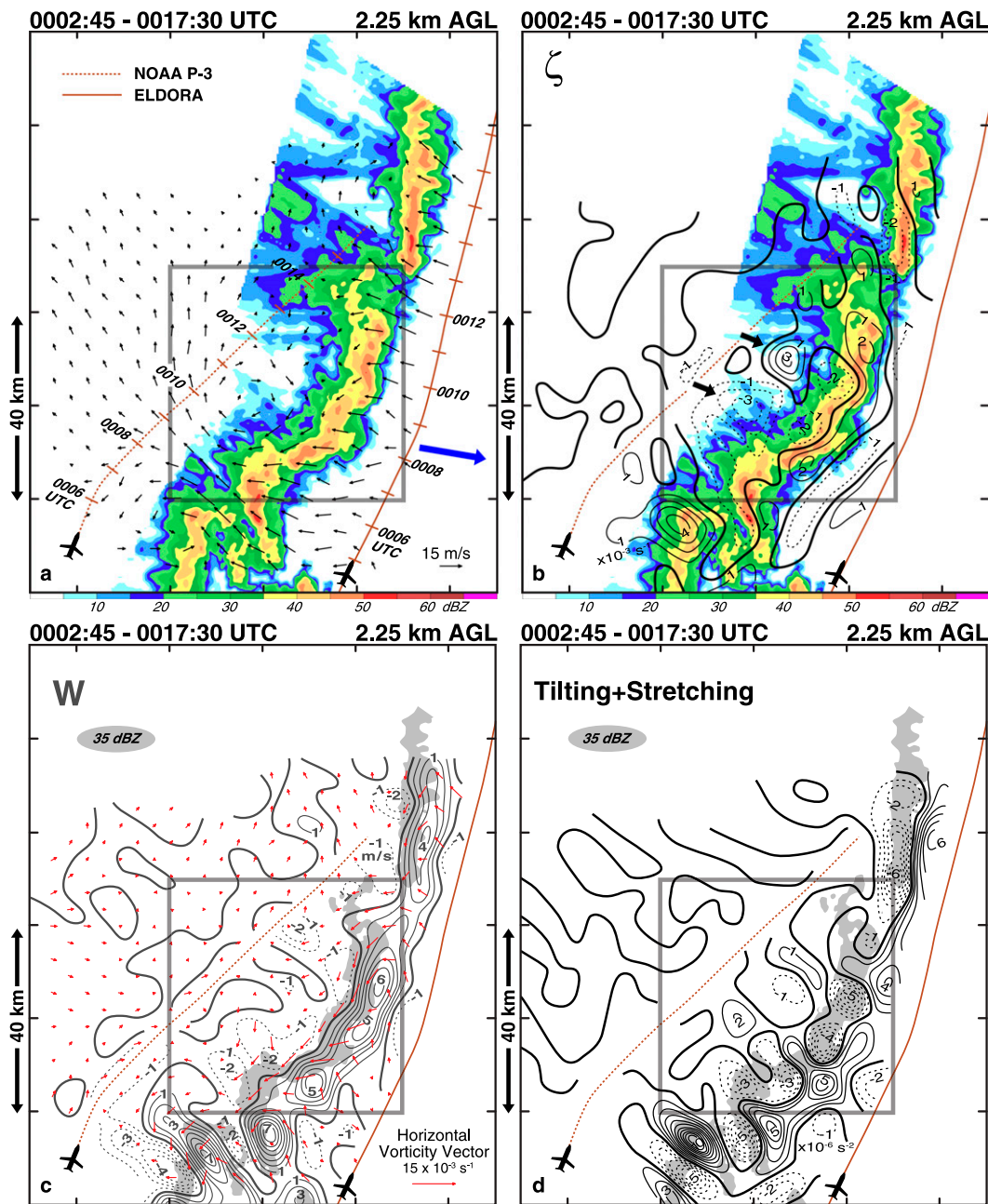
FIG. 8. Wind synthesis at 0002:45–0017:30 UTC at 2.25 km AGL. (a) Storm-relative winds and radar reflectivity. (b) Vertical vorticity ($\times 10^{-3}\,\text{s}^{-1}$) and radar reflectivity. (c) Horizontal vorticity vectors, vertical velocity, and radar reflectivities >35 dB$Z$ shaded gray. (d) Tilting plus stretching terms ($\times 10^{-6}\,\text{s}^{-2}$) and radar reflectivities >35 dB$Z$ shaded gray. ELDORA and the NOAA P-3 flight tracks are shown by the solid and dashed brown lines, respectively. Positive and negative values of vertical vorticity, vertical velocity, and tilting plus stretching terms are shown by the solid and dashed black lines, respectively. The gray box is enlarged in Fig. 13d. Blue arrow in (a) denotes the convective line motion. Black arrows in (b) denote a couplet of cyclonic and anticyclonic vertical vortices.

weaker and there is a more uniform distribution of vertical vorticity.

The mean vertical cross section perpendicular to the convective line (Fig. 9) suggests a similar structure to the one shown in Fig. 5 but weak rear inflow between the 4- and 6-km levels in the stratiform region can be seen (Figs. 9a,b). The magnitude of the vorticity vector at low levels in the plane of the cross section (Fig. 9c) is weaker in the transition zone and the vertical vorticity does not suggest a banded structure
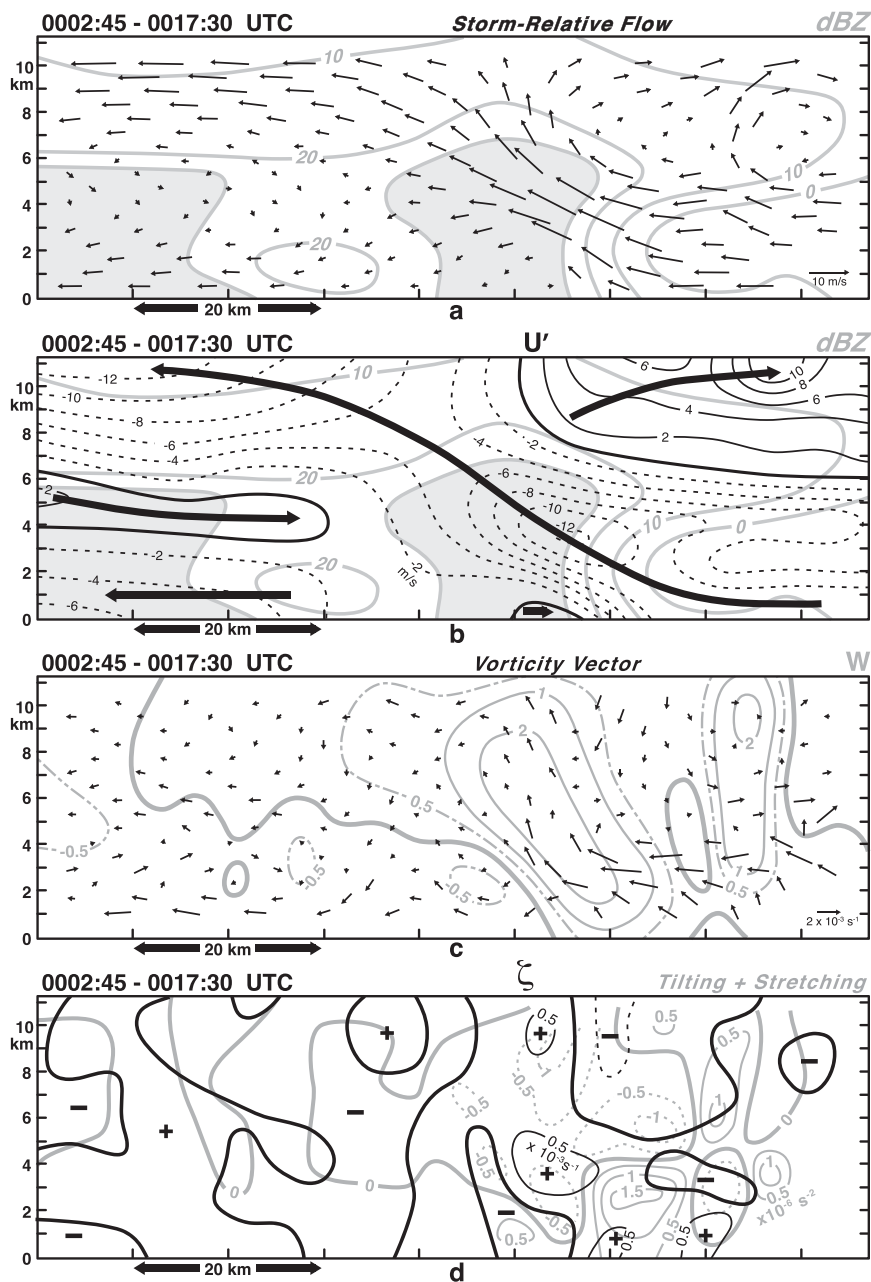
FIG. 9. Vertical cross section perpendicular to the convective line at 0002:45–0017:30 UTC depicting (a) storm-relative flow and radar reflectivity, (b) the component of storm-relative flow perpendicular to the convective line ($U'$) and radar reflectivity, (c) vorticity vector in the plane of the cross section and vertical velocity, and (d) vertical vorticity and tilting plus stretching terms. The variables are based on an average of 125 vertical cross sections along the entire length of the convective line resolved in the wind synthesis. Black arrows in (b) depict approximate flow pattern as shown in (a). To resolve areas characterized by weak gradients in (c), the 0.5 and $-0.5 \text{ m s}^{-1}$ isopleths have been added with dash–dot and dash–dot–dot lines, respectively.

similar to the plot presented in Fig. 5. Vertical velocities in the transition zone and stratiform region are also reduced compared to the earlier time. Note the low-level outflow winds (Fig. 9b), which are a reflection of the

bow-echo segment embedded within the line producing northwesterly flow near the surface at this time.

An important topic is the relationship between the BAMEX squall line that developed on 2 June 2003 and
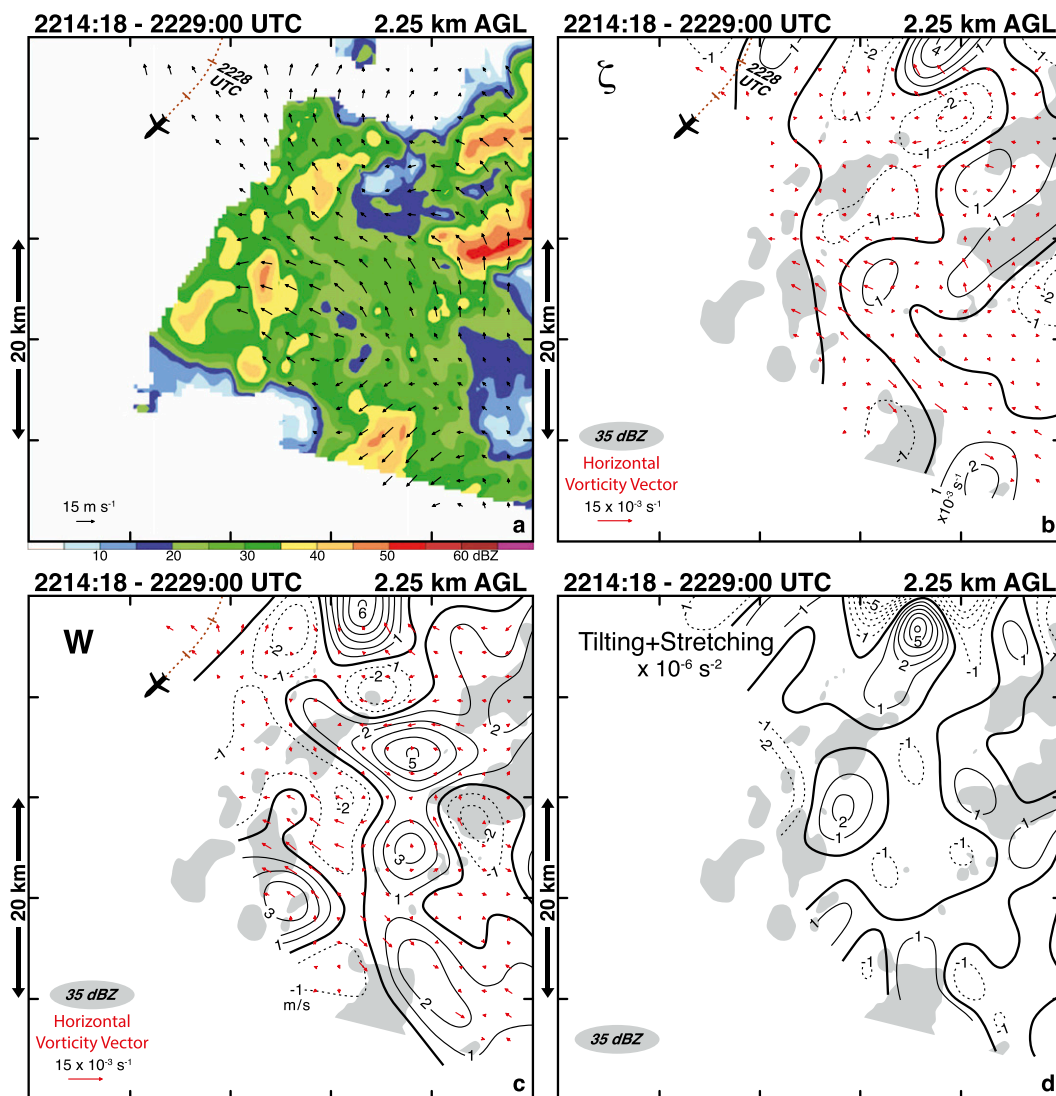
FIG. 10. Wind synthesis at 2214:18–2229:00 UTC at 2.25 km AGL. (a) Storm-relative winds and radar reflectivity. (b) Vertical vorticity ($\times 10^{-3}\,\mathrm{s}^{-1}$), horizontal vorticity vectors, and radar reflectivities >35 dB$Z$ shaded gray. (c) Horizontal vorticity vectors, vertical velocity, and radar reflectivities >35 dB$Z$ shaded gray. (d) Tilting plus stretching terms ($\times 10^{-6}\,\mathrm{s}^{-2}$) and radar reflectivities >35 dB$Z$ shaded gray. NOAA P-3 flight track is shown by the dashed brown line. Positive and negative values of vertical vorticity, vertical velocity, and tilting plus stretching are shown by the solid and dashed black lines, respectively. The area enlarged in this figure is shown by the gray box in Fig. 4.

other convective lines documented in the literature. Bluestein and Jain (1985) were the first to note that most convective lines were oriented to the left (~40°) of the vertical shear vector, suggesting that it is common for squall lines to develop in environments that contain both line-perpendicular and line-parallel vertical wind shear. This orientation angle was ~35° for the current study (Fig. 2). Parker (2007) has shown that the parallel stratiform precipitation mode associated with a convective line is preferred when there is a significant component of along-line vertical wind shear; however, the

more common trailing stratiform mode can also develop. Accordingly, the BAMEX case is not considered to be a rare event. What is perplexing is the lack of documentation of the banded vertical vorticity structure, similar to what has been presented in this study and by Biggerstaff and Houze (1991a,b). It is hypothesized that these types of vorticity features within squall-line systems are more common than previously shown. Indeed, Zhang et al. (1989) and Trier et al. (1997) have replicated the banded structure in vertical vorticity based on numerical simulations.
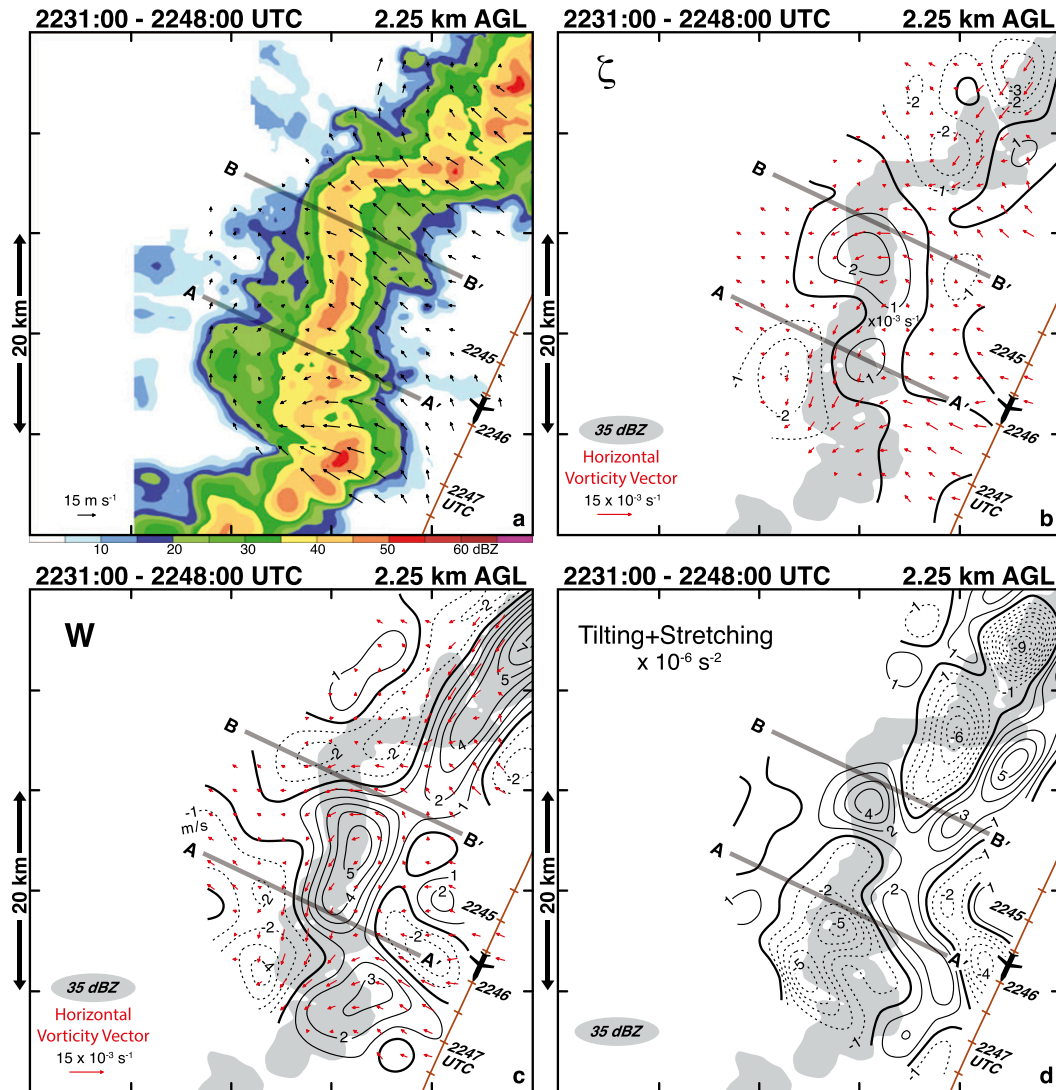
FIG. 11. Wind synthesis at 2231:00–2248:00 UTC at 2.25 km AGL. (a) Storm-relative winds and radar reflectivity. (b) Vertical vorticity ($\times 10^{-3}\,\mathrm{s}^{-1}$), horizontal vorticity vectors, and radar reflectivities $>35$ dB$Z$ shaded gray. (c) Horizontal vorticity vectors, vertical velocity, and radar reflectivities $>35$ dB$Z$ shaded gray. (d) Tilting plus stretching terms ($\times 10^{-6}\,\mathrm{s}^{-2}$) and radar reflectivities $>35$ dB$Z$ shaded gray. ELDORA flight track is shown by the brown line. Positive and negative values of vertical vorticity, vertical velocity, and tilting plus stretching are shown by the solid and dashed black lines, respectively. The area enlarged in this figure is shown by the gray box in Fig. 6. The gray lines labeled AA′ and BB′ denote the locations of vertical cross sections shown in Fig. 12.

## b. The bow echo

### AIRBORNE DOPPLER RADAR ANALYSIS

The analyses of a quasi-linear convective line presented in section 4a depict a pronounced banded structure of vertical vorticity oriented parallel to the line. This approximate two-dimensional structure changes with time as at least one segment of the line evolves into a bow echo. Embedded bow echoes or bow-shaped segments have been known to exist for a number of years (e.g., Johns and Hirt 1987); however, to date there

has not been a detailed observational examination of their life cycle. The gray box shown in Figs. 4, 6, 7, and 8 denotes the region where the bow echo develops along the convective line. As shown in Fig. 4 and as is enlarged in Fig. 10, the airborne Doppler radars were able to collect data in an area primarily associated with stratiform precipitation before the convective line organized. Accordingly, the formation of the bow echo was documented by the data collected by the radars.

The Doppler wind synthesis at 2214–2229 UTC was the first data collected on the mesoscale system and it
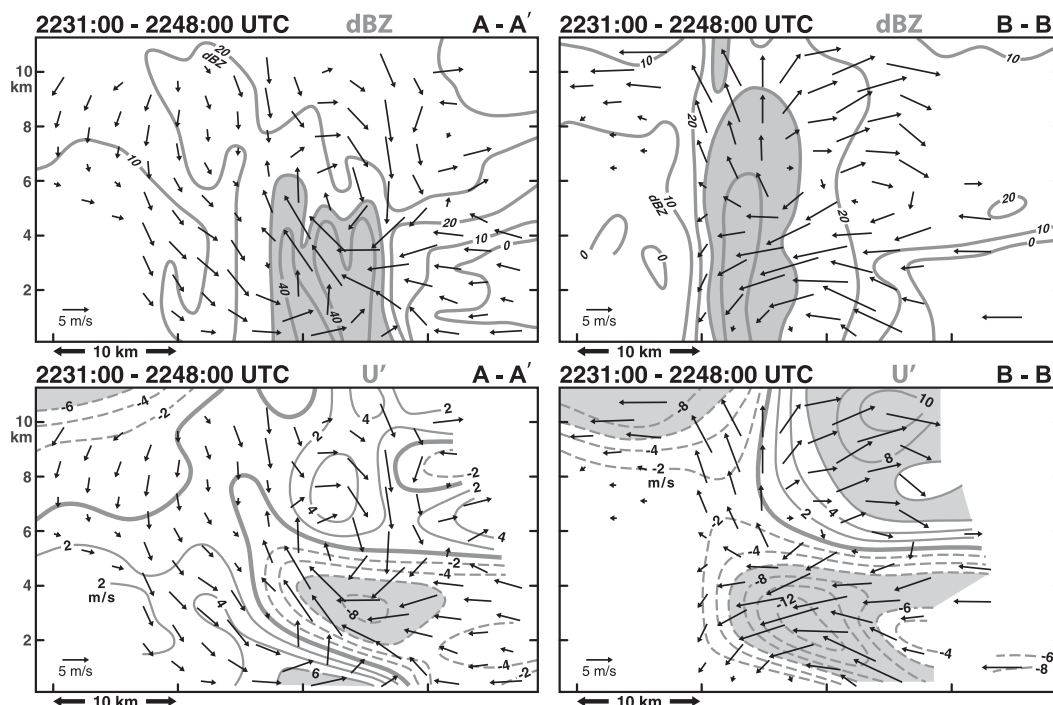
FIG. 12. Vertical cross sections perpendicular to the convective line at 2231:00–2248:00 UTC. Sections along segments (left) AA′ and (right) BB′, shown in Fig. 11. (top) The radar reflectivity (>30 dBZ shaded gray) and (bottom) the component of storm-relative flow perpendicular to the convective line ($U'$; values greater than and less than 6 and $-6\,\mathrm{m\,s^{-1}}$ are shaded gray). The storm-relative wind vectors in the plane of the cross section are also plotted.

also combined the data collected by both the ELDORA and the NOAA P-3 airborne radars. The storm-relative winds were primarily southeasterly in Fig. 10a except for the small region of northeasterly flow in the southern section of the domain. The vertical velocities were weaker owing to the general absence of an organized convective line (Fig. 10c) although the southern tip of the banded structure in the vertical vorticity, discussed in section 4a, does extend into this region as shown at the top of Fig. 10b (note the region where $\zeta > 4 \times 10^{-3}\,\mathrm{s^{-1}}$ and $w > 6\,\mathrm{m\,s^{-1}}$). The combined effects of the tilting and stretching terms were generally small in this area (Fig. 10d).

Convection formed in the region by the next aircraft pass (Fig. 11a) and is apparent by the extension of the line farther to the south. The first indication of the incipient counterrotating circulation patterns that would later lead to the formation of the embedded bow echo was evident during this analysis time. The circulation patterns are aligned southwest to northeast and the centers are separated by ~20 km (Fig. 11b). There are a number of features worth noting in Fig. 11. An updraft (>5 m s⁻¹) within the convective line has developed approximately between the two centers (Fig. 11c). The horizontal vorticity vectors within this updraft are primarily pointing to the southwest. Tilting (and

subsequent stretching) of this vorticity vector would be consistent with the development of the cyclonic and anticyclonic circulations, which is supported by the analysis of these terms in Fig. 11d (note the maximum and minimum centers within the convective lines $>4 \times 10^{-6}\,\mathrm{s^{-2}}$ and $< -5 \times 10^{-6}\,\mathrm{s^{-2}}$, respectively).

Weisman and Davis (1998) have suggested that subsystem vortices may form as a result of the upward tilting of the cold-pool-generated vorticity. James et al. (2006) have proposed that bowing segments develop in regions where the cold pool is much stronger than at other locations along the line. The analyses shown in Fig. 11 supports the tilting of horizontal vorticity generated by the cold pool owing to the northeast to southwest orientation of the vorticity vector within the updraft. The vorticity vectors point in a westerly direction farther north along the line before reorienting and pointing back to the southwest in the northeast section of the domain. These changes in the direction of the vector can be explained by variations in the cold pool strength along the convective line as hypothesized by James et al. (2006).

Two vertical cross sections perpendicular to the line were created to examine the cold pool structure. The cross section labeled AA′ is chosen at a location where
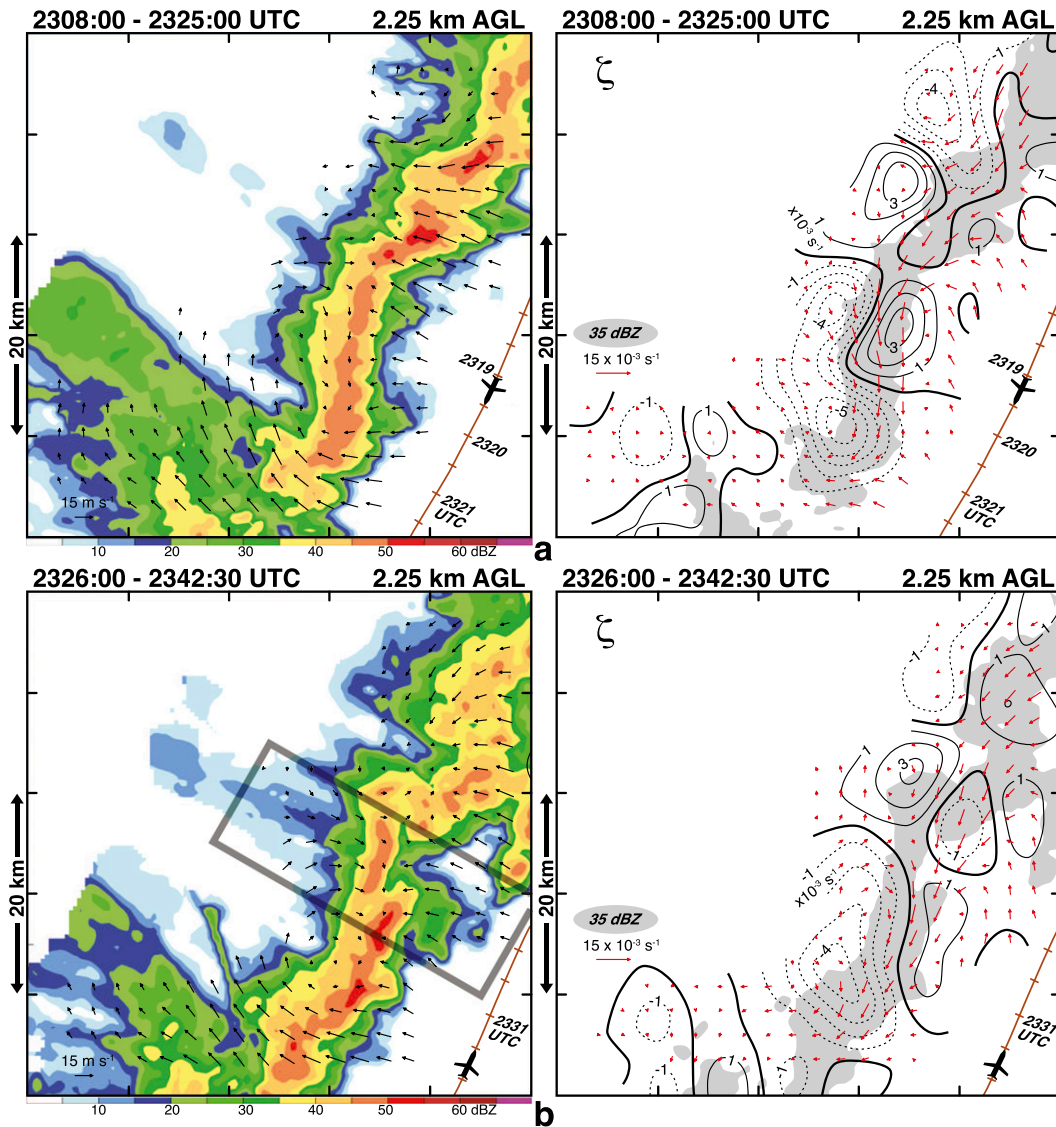
FIG. 13. Wind synthesis at (a) 2308:00–2325:00, (b) 2326:00–2342:30, (c) 2344:30–0001:30, and (d) 0002:45–0017:30 UTC at 2.25 km AGL. (left) Storm-relative winds and radar reflectivity. (right) Vertical vorticity ($\times 10^{-3}$ s$^{-1}$), horizontal vorticity vectors, and radar reflectivities >35 dBZ shaded gray. ELDORA and NOAA P-3 flight tracks are shown by the brown and dashed brown lines, respectively. Positive and negative values of vertical vorticity are shown by the solid and dashed black lines, respectively. The areas enlarged in (a) and (d) are shown by the gray box in Figs. 7 and 8, respectively. The gray box in (b) denotes the region where an along-line average shown in Fig. 15b was created.

the vorticity vectors have the greatest magnitude while directed to the southwest (Fig. 11c). The section slices through the updraft (Fig. 11c) and approximately between the two counterrotating circulations (Fig. 11b). The cross section labeled BB′ is located in the area where the vorticity vectors are pointing to the west (Fig. 11c). The storm-relative winds plotted in the left-hand panels (AA′) in Fig. 12 show the low-level outflow undercutting the inflow and leading to an upshear-tilted updraft. The negative vertical velocities at upper levels and to the rear of the convective line are associated with

the transition zone downdraft. The vertical cross section along BB′ (the right panels in Fig. 12) depicts a very shallow cold pool and weaker outflow winds as expected. Such variations in along-line cold pool strength were also documented in a narrow cold-frontal rainband (Jorgensen et al. 2003).

The evolutions of the counterrotating circulation patterns are shown based on the fourth, fifth, sixth, and seventh flight legs flown by the bow echo (Fig. 13). The orientation and magnitude of the horizontal vorticity vector along the convective line can be used as a proxy
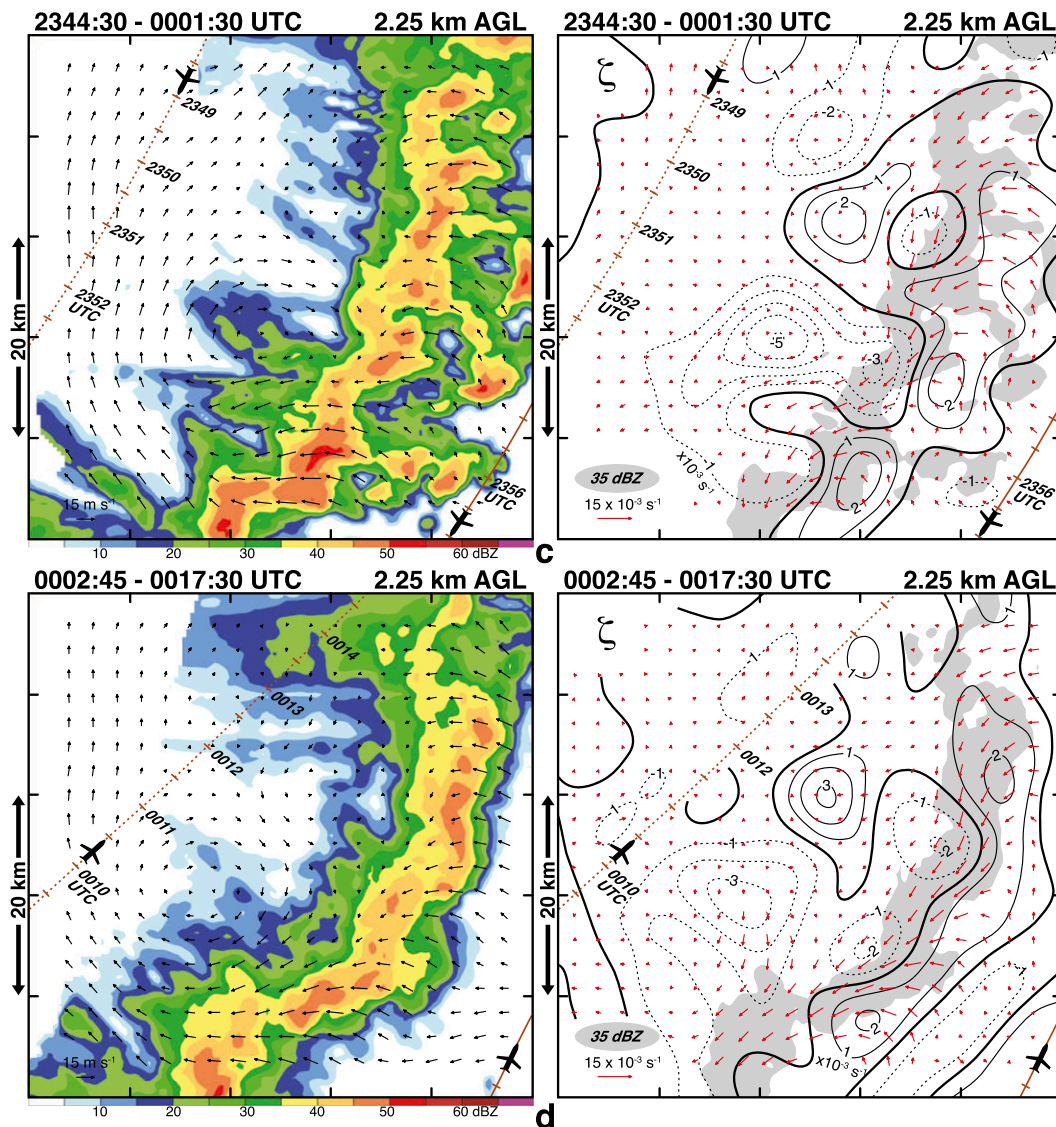
FIG. 13. (*Continued*)

for the strength of the cold pool. The vorticity vectors in Fig. 13a are primarily oriented northeast to southwest and are approximately the same magnitude, suggesting the cold pool is uniformly strong by the fourth pass (Fig. 13a). The tilting and stretching terms (not shown) continue to support the increase in intensity of the counterrotating vortices.

The vortices are persistent features in all of the times shown in Fig. 13. They are close to the convective line at the earlier times (Figs. 13a,b) and subsequently move rearward relative to the line as the echo begins to "bow out" (Figs. 13c,d). The bowing segment is clearly apparent in the echo pattern shown in Fig. 13d. A time–height plot of the maximum vorticity within the cyclonic vortex (Fig. 14) shows the low-level origin of the

circulation during the second aircraft pass. The vortex builds upward with the location of maximum vorticity reaching 4–5 km by the fourth analysis time. The ridge of maximum vorticity continues to increase in intensity ($>4 \times 10^{-3} \text{ s}^{-1}$) but slowly descends in altitude during the last two analysis times, which coincides with the movement of both cyclonic and anticyclonic circulations farther to the rear relative to the main convective line.

The evolution of the rear inflow is depicted in the mean vertical cross section perpendicular to the line (Fig. 15). These cross sections are based on an average near the bow-echo apex. There is a hint of rear inflow in the $U'$ component of the relative wind during the third aircraft pass by the system at 2250–2305 UTC (Fig. 15a). The rear inflow becomes a prominent feature by the
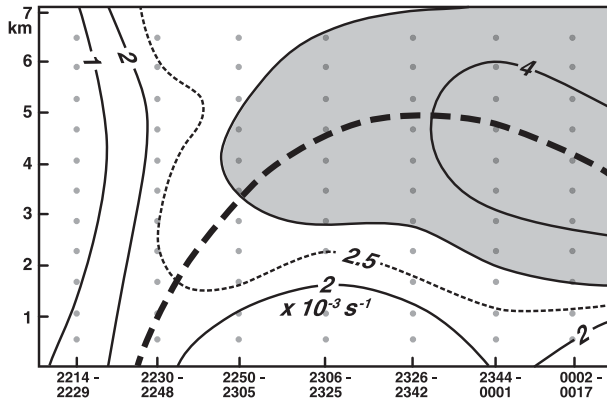
FIG. 14. Time–height cross section of the maximum vertical vorticity within the cyclonic vortex. Vorticity greater than $3 \times 10^{-3}\,\mathrm{s}^{-1}$ is shaded gray. The black dashed line represents the ridge of maximum vorticity. The gray dots represent the analysis levels.

fourth pass at 2326–2342 UTC (Fig. 15b) with continuous flow toward the front of the convective line descending to near the surface. The radar reflectivity values have decreased in magnitude near the $4\,\mathrm{m\,s^{-1}}$ isopleth in the rear inflow at 4 km. This is a characteristic feature when drier air is being advected into the convective line (e.g., Smull and Houze 1987; Przybylinski 1995). The mean updraft also strengthens during the fourth pass (not shown), which is consistent with the height of the 30-dB$Z$ isopleth extending to a higher altitude in Fig. 15b.

Weisman (1993) highlighted the role of horizontal pressure gradients produced by buoyancy in supporting the rear-inflow jet. However, the current study

emphasizes the importance of the counterrotating circulations in contributing to the intensity of the rear-inflow jet. The contribution by the wind speed in the rear-inflow jet by the bookend vortices was estimated by using the technique outlined by Wakimoto et al. (2006). They compute the nondivergent component of the wind field, which was subsequently subtracted from the multi-Doppler wind synthesis to create a modified wind field without the effect of the bookend vortices. This removal revealed that the vortices contributed ~60% to the total wind generated with the jet (not shown). Grim et al. (2009) have also shown that the dynamic pressure effects resulting from these circulations can be a significant contributor to the rear-inflow jet.

## 5. Summary and discussion

Two airborne Doppler radars collected data that documented the evolution of a quasi-linear convective line accompanied by a trailing stratiform region during BAMEX. A total of seven passes were made by the aircraft over a 2-h period. The low-level wind shear vector within the environment was associated with a significant along-line component. This resulted in an ambient horizontal vorticity vector that pointed into the convective line. The broad-scale locations of vertical motions within the convective and stratiform regions documented in the present study are consistent with previous squall-line studies. Downdrafts were located out ahead of the line, accompanying the heavy
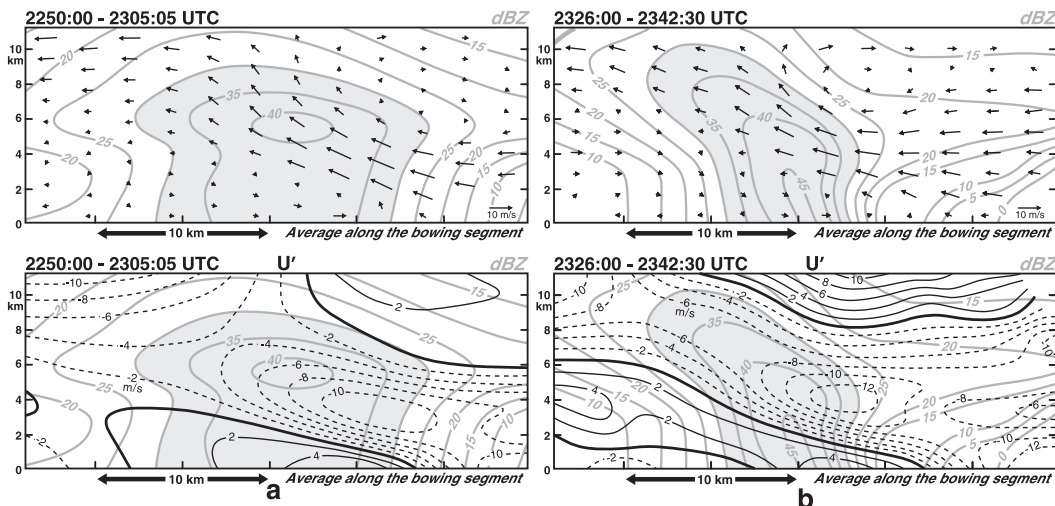
FIG. 15. Vertical cross section perpendicular to the convective line at (a) 2250:00–2305:05 and (b) 2326:00–2342:30 UTC averaged along the bowing segment of the convective line depicting (top) storm-relative flow and radar reflectivity and (bottom) the component of storm-relative flow perpendicular ($U'$) to the convective line and radar reflectivity. The variables are based on an average of 17 vertical cross sections. The location of the along-line average cross section presented in (b) is shown in Fig. 13b.
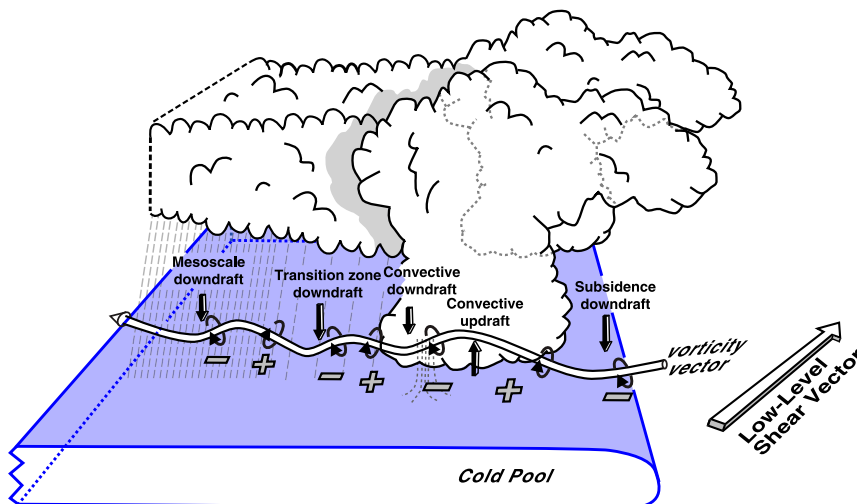
FIG. 16. Schematic model summarizing the tilting of ambient horizontal vorticity by the vertical motions within a mesoscale convective system during the early stage of development. The plus and minus signs denote the signs of vertical vorticity that are created.

precipitation within the convective line, within the transition zone, and near the brightband region where the heaviest stratiform precipitation occurs. These downdrafts and the main convective updraft tilted the horizontal vorticity vector into the vertical, producing prominent bands of cyclonic and anticyclonic vertical vorticity early in the life cycle of the convective line. Stretching also contributed to the maintenance of these bands. A schematic model summarizing the vorticity patterns that formed during the early stages of the convective line is presented in Fig. 16. The patterns shown in Fig. 16 can develop in environments characterized by both line-perpendicular and line-parallel vertical wind shear, a common situation with most convective lines (e.g., Bluestein and Jain 1985).

Interestingly, this type of vertical vorticity structure has rarely been documented in the literature. Biggerstaff and Houze (1991a,b) also noted a similar pattern using a composite analysis. Their technique was not able to resolve the subsidence downdraft out ahead of the convective line and the low-level convective downdraft although it is likely that both were present in their case study. They were also only able to analyze one time versus the numerous Doppler radar wind syntheses available in the present study.

The kinematic structure of the convective line began to deviate from the one depicted in Fig. 16 later in its life cycle. The embedded bow echo that developed and intensified during the observational period contributed to the convective line evolving into a more three-dimensional pattern. A detailed observational analysis of this type of bow echo has not been previously reported in the

literature. Weisman (1993) had originally proposed that tilting of ambient horizontal vorticity was the dominant mechanism for producing bookend vortices associated with bow echoes but could not rule out the possible contribution of convectively generated horizontal vorticity. Weisman and Davis (1998) suggested that subsystem bow echoes within a convective line were created by tilting of cold-pool-generated horizontal vorticity. The results presented in this study support the latter hypothesis and reveal the importance of along-frontal variability in the depth of the cold pool in determining preferred locations where the embedded bow echo can form. The deep outflows lead to the production of a horizontal vortex with sufficient magnitude and orientation such that tilting and subsequent stretching produced a prominent couplet of vertical vorticity. It was estimated that ~60% of the total wind speed generated by the rear-inflow jet was attributed to these counterrotating circulation patterns. James et al. (2006) proposed that the growth of bow-echo structures within a linear convective system appears to depend critically on the local strengthening of the cold pool to the extent that the convection becomes locally upshear tilted. A positive feedback process is thereby initiated, allowing the intensification of the bow echo. The present study has shown that the formation of the counterrotating circulations is also important to the formation of the embedded bow echo by contributing to the total wind speed of the rear-inflow jet. The schematic model (Fig. 17) depicts the differential depth in the cool outflow along the quasilinear convective line. The bow echo results from the development of a rear-inflow jet. The jet is largely driven
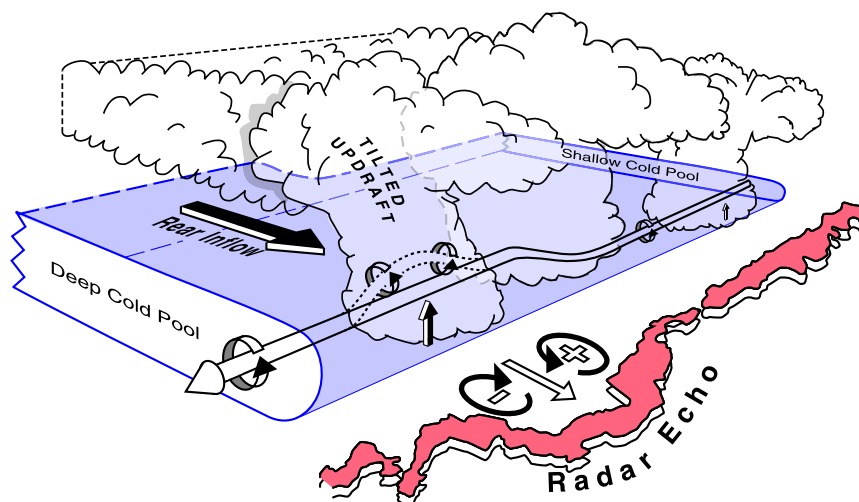
FIG. 17. Schematic model illustrating the development of the counterrotating circulations that contribute to the development of a subsystem or embedded bow echo. These circulations preferentially form at a local region where the cold pool is deep. Updrafts tilt the horizontal vorticity produced within the leading edge of the cold pool producing the counterrotating circulations. The circulations promote the development of a rear-inflow jet that is also augmented by the upshear-tilted updraft. Radar echo depiction of the embedded bow echo that develops is shown by the red-shaded region in the schematic.

by the combined effects of the counterrotating vortices created by the tilting of the horizontal vorticity produced by the cold pool and the upshear-tilted updraft.

It should be noted that the preference for embedded bow echoes to form in regions of locally enhance cold pools described by James et al. (2006) and the present study is not the only possible generating mechanism. An embedded bow echo could hypothetically develop if a stronger convective cell within a convective line associated with intense updrafts formed in a region of uniform horizontal vorticity. The latter scenario could develop as a result of a localized maximum in CAPE or enhanced convergence owing to a preexisting low-level boundary or terrain effects.

Future studies should focus on convective lines with trailing stratiform regions that develop in environments where the ambient low-level wind shear vector has a major component along the line. These types of mesoscale convective systems appear to develop a kinematic structure in vertical vorticity that has rarely been documented in the literature (e.g., Biggerstaff and Houze 1991a,b). Indeed, the plethora of numerical simulations of convective lines have only occasionally shown these features. Additional studies of embedded bow echoes would also help assess the generality of the results presented in this paper.

## APPENDIX

### Radar Data Synthesis

The ELDORA and NOAA P-3 data were edited and the aircraft motion was removed from the velocity data using the Solo software package (Oye et al. 1995). The technique developed by Testud et al. (1995) was used to correct for navigation errors. The along-track data spacing and sweep-angle beam spacing for ELDORA were ~300 m and 1.4°, respectively. These resolutions led to an effective sampling of ~600 m in the vertical for the distances from the radar used in this study. Accordingly, the ELDORA-only wind syntheses were interpolated onto a grid with horizontal and vertical grid spacing of 400 and 600 m, respectively. For the analyses that merged ELDORA and NOAA P-3 data, the interpolation grid was 1.2 km in the horizontal by 600 m in the vertical. The data were time–space adjusted to account for the overall storm motion (260° at 15 m s$^{-1}$). A Cressman filter (Cressman 1959) was applied during the interpolation process with a radius of influence of 400 m

in the horizontal and 600 m in the vertical (1200 and 600 m in the enlarged analysis). Sensitivity studies with larger radii of influence did not significantly alter the results. The lowest level was chosen to be at 450 m AGL.

The synthesis of the radar data was performed using the Custom Editing and Display of Reduced Information in Cartesian Space (CEDRIC; Mohr et al. 1986). A four-step Leise filter (Leise 1982) was applied to the Doppler wind field. The filter effectively removes wavelengths less than ~6 km. A three-step Leise filter was applied to the combined ELDORA and P-3 analysis, which effectively removes wavelengths less than ~5 km. The hydrometeor fall speeds were estimated from the reflectivity terminal fall speed relationship established by Joss and Waldvogel (1970) with a correction for the effects of air density (Foote and duToit 1969). Vertical velocities were obtained from horizontal convergence in a variational sense (O'Brien 1970) such that an integration of the anelastic continuity equation met both the upper and lower boundary conditions of $w = 0 \, \mathrm{m \, s^{-1}}$.

The NOAA P-3 and ELDORA flew coordinated legs during the first, third, sixth, and seventh passes along the convective line. The merger of the dataset produced a synthesized wind field that covered both the convective and stratiform regions of the mesoscale convective system. The merged radar reflectivity data were not shown for these four passes in the horizontal plots presented in the manuscript. It was decided to present only the ELDORA radar reflectivity analysis in order to facilitate the comparisons between all of the plots. The vertical cross sections of radar reflectivity presented in Figs. 5 and 9, however, are based on the merged datasets collected by both aircraft.

## REFERENCES

Bartels, D. L., and R. A. Maddox, 1991: Midlevel cyclonic vortices generated by mesoscale convective complexes. *Mon. Wea. Rev.,* **119,** 104–118, doi:10.1175/1520-0493(1991)119<0104: MCVGBM>2.0.CO;2.

Biggerstaff, M. I., and R. A. Houze Jr., 1991a: Kinematic and precipitation structure of the 10–11 June 1985 squall line. *Mon. Wea. Rev.,* **119,** 3034–3065, doi:10.1175/1520-0493(1991)119<3034: KAPSOT>2.0.CO;2.

——, and ——, 1991b: Midlevel vorticity structure of the 10–11 June 1985 squall line. *Mon. Wea. Rev.,* **119,** 3066–3079, doi:10.1175/ 1520-0493(1991)119<3066:MVSOTJ>2.0.CO;2.

Bluestein, H. B., and M. H. Jain, 1985: Formation of mesoscale lines of precipitation: Nonsevere squall lines in Oklahoma during the spring. *Mon. Wea. Rev.,* **115,** 2719–2727, doi:10.1175/ 1520-0493(1987)115<2719:FOMLOP>2.0.CO;2.

Bosart, L. F., and F. Sanders, 1981: The Johnstown flood of July 1977: A long-lived convective system. *J. Atmos. Sci.,* **38,** 1616–1642, doi:10.1175/1520-0469(1981)038<1616: TJFOJA>2.0.CO;2.

Coniglio, M. C., D. J. Stensrud, and M. B. Richman, 2004: An observational study of derecho-producing convective storms. *Wea. Forecasting,* **19,** 320–337, doi:10.1175/1520-0434(2004)019<0320: AOSODC>2.0.CO;2.

Cressman, G. P., 1959: An operational objective analysis system. *Mon. Wea. Rev.,* **87,** 367–374, doi:10.1175/1520-0493(1959)087<0367: AOOAS>2.0.CO;2.

Davis, C. A., and M. L. Weisman, 1994: Balanced dynamics of mesoscale vortices produced in simulated convective systems. *J. Atmos. Sci.,* **51,** 2005–2030, doi:10.1175/1520-0469(1994)051<2005: BDOMVP>2.0.CO;2.

——, and S. B. Trier, 2002: Cloud-resolving simulations of mesoscale vortex intensification and its effect on a serial mesoscale convective system. *Mon. Wea. Rev.,* **130,** 2839–2858, doi:10.1175/ 1520-0493(2002)130<2839:CRSOMV>2.0.CO;2.

——, and Coauthors, 2004: The Bow Echo and MCV Experiment. *Bull. Amer. Meteor. Soc.,* **85,** 1075–1093, doi:10.1175/ BAMS-85-8-1075.

Evans, J. S., and C. A. Doswell III, 2001: Examination of derecho environments using proximity soundings. *Wea. Forecasting,* **16,** 329– 342, doi:10.1175/1520-0434(2001)016<0329:EODEUP>2.0.CO;2.

Fankhauser, J. C., G. M. Barnes, and M. A. LeMone, 1992: Structure of a midlatitude squall line formed in strong unidirectional shear. *Mon. Wea. Rev.,* **120,** 237–260, doi:10.1175/ 1520-0493(1992)120<0237:SOAMSL>2.0.CO;2.

Foote, G. B., and P. S. du Toit, 1969: Terminal velocity of raindrops aloft. *J. Appl. Meteor.,* **8,** 249–253, doi:10.1175/1520-0450(1969)008<0249: TVORA>2.0.CO;2.

Fritsch, J. M., J. D. Murphy, and J. S. Kain, 1994: Warm core vortex amplification over land. *J. Atmos. Sci.,* **51,** 1780–1807, doi:10.1175/ 1520-0469(1994)051<1780:WCVAOL>2.0.CO;2.

Fujita, T. T., 1981: Tornadoes and downbursts in the context of generalized planetary scales. *J. Atmos. Sci.,* **38,** 1511–1534, doi:10.1175/1520-0469(1981)038<1511:TADITC>2.0.CO;2.

Grim, J. A., R. M. Rauber, G. M. McFarquhar, and B. F. Jewett, 2009: Development and forcing of the rear inflow jet in a rapidly developing and decaying squall line during BAMEX. *Mon. Wea. Rev.,* **137,** 1206–1229, doi:10.1175/ 2008MWR2503.1.

Hildebrand, P. H., C. A. Walther, C. L. Frush, J. Testud, and F. Baudin, 1994: The ELDORA/ASTRAIA airborne Doppler weather radar: Goals, design and first field tests. *Proc. IEEE,* **82,** 1873–1890, doi:10.1109/5.338076.

——, and Coauthors, 1996: The ELDORA/ASTRAIA airborne Doppler weather radar: High-resolution observations from TOGA COARE. *Bull. Amer. Meteor. Soc.,* **77,** 213–232, doi:10.1175/1520-0477(1996)077<0213:TEADWR>2.0.CO;2.

Houze, R. A., Jr., S. A. Rutledge, M. I. Biggerstaff, and B. F. Smull, 1989: Interpretation of Doppler weather radar displays of midlatitude mesoscale convective systems. *Bull. Amer. Meteor. Soc.,* **70,** 608–619, doi:10.1175/1520-0477(1989)070<0608: IODWRD>2.0.CO;2.

——, B. F. Smull, and P. Dodge, 1990: Mesoscale organization of springtime rainstorms in Oklahoma. *Mon. Wea. Rev.,* **118,** 613–654, doi:10.1175/1520-0493(1990)118<0613: MOOSRI>2.0.CO;2.

Hoxit, L. R., C. F. Chappell, and J. M. Fritsch, 1976: Formation of mesolows or pressure troughs in advance of cumulonimbus clouds. *Mon. Wea. Rev.,* **104,** 1419–1428, doi:10.1175/ 1520-0493(1976)104<1419:FOMOPT>2.0.CO;2.

James, R. P., P. M. Markowski, and J. M. Fritsch, 2006: Bow echo sensitivity to ambient moisture and cold pool strength. *Mon. Wea. Rev.,* **134,** 950–964, doi:10.1175/MWR3109.1.

Johns, R. H., 1993: Meteorological conditions associated with bow echo development in convective storms. *Wea. Forecasting,* **8,** 294–299, doi:10.1175/1520-0434(1993)008<0294:MCAWBE>2.0.CO;2.

——, and W. D. Hirt, 1987: Derechos: Widespread convectively induced windstorms. *Wea. Forecasting,* **2,** 32–49, doi:10.1175/1520-0434(1987)002<0032:DWCIW>2.0.CO;2.

Jorgensen, D. P., P. H. Hildebrand, and C. L. Frush, 1983: Feasibility test of an airborne pulse-Doppler meteorological radar. *J. Climate Appl. Meteor.,* **22,** 744–757, doi:10.1175/1520-0450(1983)022<0744:FTOAAP>2.0.CO;2.

——, T. Matejka, and J. D. DuGranut, 1996: Multi-beam techniques for deriving wind fields from airborne Doppler radars. *J. Meteor. Atmos. Phys.,* **59,** 83–104, doi:10.1007/BF01032002.

——, M. A. LeMone, and S. B. Trier, 1997: Structure and evolution of the 22 February 1993 TOGA COARE squall line: Aircraft observations of precipitation, circulation, and surface energy fluxes. *J. Atmos. Sci.,* **54,** 1961–1985, doi:10.1175/1520-0469(1997)054<1961:SAEOTF>2.0.CO;2.

——, Z. Pu, P. O. G. Persson, and W.-K. Tao, 2003: Variations associated with cores and gaps of a Pacific narrow cold frontal rainband. *Mon. Wea. Rev.,* **131,** 2705–2729, doi:10.1175/1520-0493(2003)131<2705:VAWCAG>2.0.CO;2.

Joss, J., and D. Waldvogel, 1970: Raindrop size distribution and Doppler velocities. Preprints, *14th Conf. on Radar Meteorology,* Tucson, AZ, Amer. Meteor. Soc., 153–156.

Keenan, T. D., and R. E. Carbone, 1992: A preliminary morphology of precipitation systems in tropical northern Australia. *Quart. J. Roy. Meteor. Soc.,* **118,** 283–326, doi:10.1002/qj.49711850406.

Klimowski, B. A., M. R. Hjelmfelt, and M. J. Bunkers, 2004: Radar observations of the early evolution of bow echoes. *Wea. Forecasting,* **19,** 727–734, doi:10.1175/1520-0434(2004)019<0727:ROOTEE>2.0.CO;2.

Leise, J. A., 1982: A multidimensional scale-telescoped filter and data extension package. NOAA Tech. Memo. ERL WPL-82, 19 pp. [Available from NOAA ERL, 325 Broadway, Boulder, CO 80303.]

Mohr, C. G., L. J. Miller, R. L. Vaughn, and H. W. Frank, 1986: The merger of mesoscale datasets into a common Cartesian format for efficient and systematic analysis. *J. Atmos. Oceanic Technol.,* **3,** 143–161, doi:10.1175/1520-0426(1986)003<0143:TMOMDI>2.0.CO;2.

O'Brien, J. J., 1970: Alternative solutions to the classical vertical velocity problem. *J. Appl. Meteor.,* **9,** 197–203, doi:10.1175/1520-0450(1970)009<0197:ASTTCV>2.0.CO;2.

Oye, R., C. Mueller, and S. Smith, 1995: Software for radar translation, visualization, editing and interpolation. Preprints, *27th Conf. on Radar Meteorology,* Vail, CO, Amer. Meteor. Soc., 359–364.

Parker, M. D., 2007: Simulated convective lines with parallel stratiform precipitation. Part I: An archetype for convection in along-line shear. *J. Atmos. Sci.,* **64,** 267–288, doi:10.1175/JAS3853.1.

——, and R. H. Johnson, 2000: Organizational modes of midlatitude mesoscale convective systems. *Mon. Wea. Rev.,* **128,** 3413–3436, doi:10.1175/1520-0493(2001)129<3413:OMOMMC>2.0.CO;2.

Przybylinski, R. W., 1995: The bow echo: Observations, numerical simulations, and severe weather detection methods. *Wea. Forecasting,* **10,** 203–218, doi:10.1175/1520-0434(1995)010<0203:TBEONS>2.0.CO;2.

Robe, F., and K. A. Emanuel, 2001: The effect of vertical wind shear on radiative–convective equilibrium states. *J. Atmos. Sci.,* **58,** 1427–1445, doi:10.1175/1520-0469(2001)058<1427:TEOVWS>2.0.CO;2.

Rotunno, R., J. B. Klemp, and M. L. Weisman, 1988: A theory for strong, long-lived squall lines. *J. Atmos. Sci.,* **45,** 463–485, doi:10.1175/1520-0469(1988)045<0463:ATFSLL>2.0.CO;2.

Skamarock, W. C., M. L. Weisman, and J. B. Klemp, 1994: Three-dimensional evolution of simulated long-lived squall lines. *J. Atmos. Sci.,* **51,** 2563–2584, doi:10.1175/1520-0469(1994)051<2563:TDEOSL>2.0.CO;2.

Smull, B. F., and R. A. Houze Jr., 1987: Rear inflow in squall lines with trailing stratiform precipitation. *Mon. Wea. Rev.,* **115,** 2869–2889, doi:10.1175/1520-0493(1987)115<2869:RIISLW>2.0.CO;2.

Sun, J., S. Braun, M. I. Biggerstaff, R. G. Fovell, and R. A. Houze Jr., 1993: Warm upper-level downdrafts associated with a squall line. *Mon. Wea. Rev.,* **121,** 2919–2927, doi:10.1175/1520-0493(1993)121<2919:WULDAW>2.0.CO;2.

Testud, J., P. H. Hildebrand, and W.-C. Lee, 1995: A procedure to correct airborne Doppler radar data for navigation errors using the echo returned from the earth's surface. *J. Atmos. Oceanic Technol.,* **12,** 800–820, doi:10.1175/1520-0426(1995)012<0800:APTCAD>2.0.CO;2.

Trier, S. B., W. C. Skamarock, and M. A. LeMone, 1997: Structure and evolution of the 22 February 1993 TOGA COARE squall line: Organization mechanisms inferred from numerical simulations. *J. Atmos. Sci.,* **54,** 386–407, doi:10.1175/1520-0469(1997)054<0386:SAEOTF>2.0.CO;2.

Verlinde, J., and W. R. Cotton, 1990: A mesoscale vortex couplet observed in the trailing anvil of a multicellular convective complex. *Mon. Wea. Rev.,* **118,** 993–1010, doi:10.1175/1520-0493(1990)118<0993:AMVCOI>2.0.CO;2.

Wakimoto, R. M., H. V. Murphey, C. A. Davis, and N. T. Atkins, 2006: High winds generated by bow echoes. Part II: The relationship between the mesovortices and damaging straight-line winds. *Mon. Wea. Rev.,* **134,** 2813–2829, doi:10.1175/MWR3216.1.

Weckwerth, T. M., and R. M. Wakimoto, 1992: The initiation and organization of convective cells atop a cold-air outflow boundary. *Mon. Wea. Rev.,* **120,** 2169–2187, doi:10.1175/1520-0493(1992)120<2169:TIAOOC>2.0.CO;2.

Weisman, M. L., 1992: The role of convectively generated rear-inflow jets in the evolution of long-lived mesoconvective systems. *J. Atmos. Sci.,* **49,** 1826–1847, doi:10.1175/1520-0469(1992)049<1826:TROCGR>2.0.CO;2.

——, 1993: The genesis of severe, long-lived bow echoes. *J. Atmos. Sci.,* **50,** 645–670, doi:10.1175/1520-0469(1993)050<0645:TGOSLL>2.0.CO;2.

——, 2001: Bow echoes: A tribute to T. T. Fujita. *Bull. Amer. Meteor. Soc.,* **82,** 97–116, doi:10.1175/1520-0477(2001)082<0097:BEATTT>2.3.CO;2.

——, and C. A. Davis, 1998: Mechanisms for the generation of mesoscale vortices within quasi-linear convective systems. *J. Atmos. Sci.,* **55,** 2603–2622, doi:10.1175/1520-0469(1998)055<2603:MFTGOM>2.0.CO;2.

——, J. B. Klemp, and R. Rotunno, 1988: Structure and evolution of numerically simulated squall lines. *J. Atmos. Sci.,* **45,** 1990–2013, doi:10.1175/1520-0469(1988)045<1990:SAEONS>2.0.CO;2.

Zhang, D.-L., K. Gao, and D. B. Parsons, 1989: Numerical simulation of an intense squall line during 10–11 June 1985 PRE-STORM. Part I: Model verification. *Mon. Wea. Rev.,* **117,** 960–994, doi:10.1175/1520-0493(1989)117<0960:NSOAIS>2.0.CO;2.